

1 **Simulating CH₄ and CO₂ over South and East Asia using the zoomed**
2 **chemistry transport model LMDzINCA**

3 Xin Lin¹, Philippe Ciais¹, Philippe Bousquet¹, Michel Ramonet¹, Yi Yin¹, Yves Balkanski¹,
4 Anne Cozic¹, Marc Delmotte¹, Nikolaos Evangeliou², Nuggehalli K. Indira³, Robin
5 Locatelli^{1a}, Shushi Peng⁴, Shilong Piao⁴, Marielle Saunois¹, Panangady S. Swathi³, Rong
6 Wang¹, Camille Yver-Kwok¹, Yogesh K. Tiwari⁵, Lingxi Zhou⁶

7

8

9

10 Affiliations:

11 ¹Laboratoire des Sciences du Climat et de l'Environnement, LSCE-IPSL (CEA-CNRS-
12 UVSQ), Université Paris-Saclay, 91191 Gif-sur-Yvette, France

13 ²Norwegian Institute for Air Research (NILU), Department of Atmospheric and Climate
14 Research (ATMOS), Kjeller, Norway

15 ³CSIR Fourth Paradigm Institute (formerly CSIR Centre for Mathematical Modelling and
16 Computer Simulation), NAL Belur Campus, Bengaluru 560 037, India

17 ⁴Sino-French Institute for Earth System Science, College of Urban and Environmental
18 Sciences, Peking University, Beijing 100871, China

19 ⁵Centre for Climate Change Research, Indian Institute of Tropical Meteorology, Pune, India

20 ⁶Chinese Academy of Meteorological Sciences (CAMS), China Meteorological
21 Administration (CMA), Beijing, China

22

23 *Correspondence to:* X. Lin (xin.lin@lsce.ipsl.fr)

24

25 ^a Now at: AXA Global P&C, Paris, France

26 **Abstract**

27 The increasing availability of atmospheric measurements of greenhouse gases (GHGs) from
28 surface stations can improve the retrieval of their fluxes at higher spatial and temporal
29 resolutions by inversions, provided that transport models are able to properly represent the
30 variability of concentrations observed at different stations. South and East Asia (SEA) is a
31 region with large and very uncertain emissions of carbon dioxide (CO₂) and methane (CH₄),
32 the most potent anthropogenic GHGs. Monitoring networks have expanded greatly during the
33 past decade in this region, which should contribute to reducing uncertainties in estimates of
34 regional GHG budgets. In this study, we simulate concentrations of CH₄ and CO₂ using a
35 zoomed version (abbreviated as ‘ZAs’) of the global chemistry transport model LMDzINCA,
36 which has fine horizontal resolutions of ~0.66° in longitude and ~0.51° in latitude over SEA
37 and coarser resolutions elsewhere. The concentrations of CH₄ and CO₂ simulated from ZAs
38 are compared to those from the same model but with standard model grids of 2.50° in
39 longitude and 1.27° in latitude (abbreviated as ‘STs’), both prescribed with the same natural
40 and anthropogenic fluxes. Model performance is evaluated for each model version at multi-
41 annual, seasonal, synoptic and diurnal scales, against a unique observation dataset including
42 39 global and regional stations over SEA and around the world. Results show that ZAs
43 improve the overall representation of CH₄ annual gradients between stations in SEA, with
44 reduction of RMSE by 16–20% compared to STs. The model improvement mainly results
45 from reduction in representation error at finer horizontal resolutions and thus better
46 characterization of the CH₄ concentration gradients related to scatterly distributed emission
47 sources. However, the performance of ZAs at a specific station as compared to STs is more
48 sensitive to errors in meteorological forcings and surface fluxes, especially when short-term
49 variabilities or stations close to source regions are examined. This emphasizes importance of
50 accurate a priori CH₄ surface fluxes in high resolution transport modelling and inverse studies,
51 particularly regarding locations and magnitudes of emission hotspots. Model performance for
52 CO₂ suggests that the CO₂ surface fluxes have not been prescribed with sufficient accuracy
53 and resolution, especially the spatio-temporally varying carbon exchange between land
54 surface and atmosphere. Besides, representation of the CH₄ and CO₂ short-term variabilities
55 is also limited by model’s ability to simulate boundary layer mixing and mesoscale transport
56 in complex terrains, emphasizing the need to improve sub-grid physical parameterizations in
57 addition to refinement of model resolutions.

58 **1 Introduction**

59 Despite attrition in the global network of greenhouse gas (GHG) monitoring stations
60 (Houweling et al., 2012), new surface stations have been installed since the late 2000s in the
61 northern industrialized continents such as Europe (e.g., Aalto et al., 2007; Biraud et al., 2000;
62 Haszpra, 1995; Levin et al., 1995; Lopez et al., 2015; Popa et al., 2010), North America (e.g.,
63 Bakwin et al., 1998; Dlugokencky et al., 1995; Miles et al., 2012), and Northeast Asia (e.g.,
64 Fang et al., 2014; Sasakawa et al., 2010; Wada et al., 2011; Winderlich et al., 2010). In
65 particular, the number of continuous monitoring stations over land has increased (e.g., Aalto
66 et al., 2007; Bakwin et al., 1998; Lopez et al., 2015; Winderlich et al., 2010) given that more
67 stable and precise instruments are available (e.g., Yver Kwok et al., 2015). These
68 observations can be assimilated in inversion frameworks that combine them with a chemistry
69 transport model and prior knowledge of fluxes to optimize GHG sources and sinks (Berchet
70 et al., 2015; Bergamaschi et al., 2010, 2015, Bousquet et al., 2000, 2006; Bruhwiler et al.,
71 2014; Gurney et al., 2002; Peters et al., 2010; Rödenbeck et al., 2003). Given the increasing
72 observation availability, GHG budgets are expected to be retrieved at finer spatial and
73 temporal resolutions by atmospheric inversions if the atmospheric GHG variability can be
74 properly modeled at these scales. A first step of any source optimization is to evaluate the
75 ability of chemistry transport models to represent the variabilities of GHG concentrations, as
76 transport errors are recognized as one of the main uncertainties in atmospheric inversions
77 (Locatelli et al., 2013).

78 Many studies have investigated regional and local variations of atmospheric GHG
79 concentrations using atmospheric chemistry transport models, with spatial resolutions ranging
80 100–300 km for global models (e.g., Chen and Prinn, 2005; Feng et al., 2011; Law et al.,
81 1996; Patra et al., 2009a, 2009b) and 10–100 km for regional models (e.g., Aalto et al., 2006;
82 Chevillard et al., 2002; Geels et al., 2004; Wang et al., 2007). Model intercomparison
83 experiments showed that the atmospheric transport models with higher horizontal resolutions
84 are more capable of capturing the observed short-term variability at continental sites (Geels et
85 al., 2007; Law et al., 2008; Maksyutov et al., 2008; Patra et al., 2008; Saeki et al., 2013), due
86 to reduction of representation errors (point measured versus gridbox-averaged modeled
87 concentrations), improved model transport, and more detailed description of surface fluxes
88 and topography (Patra et al., 2008). However, a higher horizontal model resolution also

89 demands high-quality meteorological forcings and prescribed surface fluxes as boundary
90 conditions (Locatelli et al., 2015a).

91 Two main approaches have been deployed, in an Eulerian modeling context, to address the
92 need for high-resolution transport modeling of long-lived GHGs. The first approach is to
93 define a high-resolution grid mesh in a limited spatial domain of interest, and to nest it within
94 a global model with varying degrees of sophistication to get boundary conditions for the
95 GHGs advected inside/outside the regional domain (Bergamaschi et al., 2005, 2010; Krol et
96 al., 2005; Peters et al., 2004). The second approach is to stretch the grid of a global model
97 over a specific region (the so-called ‘zooming’) while maintaining all parameterizations
98 consistent (Hourdin et al., 2006). For the former approach, several nested high-resolution
99 zooms can be embedded into the same model (Krol et al., 2005) to focus on different regions.
100 The ‘zooming’ approach has the advantage to avoid the nesting problems (e.g., tracers
101 discontinuity, transport parameterization inconsistency) at the boundaries between a global
102 and a regional model. In this study, we use the zooming capability of the LMDz model
103 (Hourdin et al., 2006).

104 South and East Asia (hereafter ‘SEA’) has been the largest anthropogenic GHG emitting
105 region since the mid 2000s due to its rapid socioeconomic development (Boden et al., 2015;
106 Olivier et al., 2015; Le Quéré et al., 2015; Tian et al., 2016). Compared to Europe and North
107 America where sources and sinks of GHGs are partly constrained by atmospheric
108 observational networks, the quantification of regional GHG fluxes over SEA from
109 atmospheric inversions remains uncertain because of the low density of surface observations
110 (e.g., Patra et al., 2013; Swathi et al., 2013; Thompson et al., 2014, 2016). During the past
111 decade, a number of new surface stations have been deployed (e.g., Fang et al., 2016, 2014;
112 Ganesan et al., 2013; Lin et al., 2015; Tiwari and Kumar, 2012), which have the potential to
113 provide new and useful constraints on estimates of GHG fluxes in this region. However,
114 modeling GHG concentrations at these stations is challenging since they are often located in
115 complex terrains (e.g. coasts or mountains) or close to large local sources of multiple origins.
116 To fully take advantage of the new surface observations in SEA, forward modeling studies
117 based on high-resolution transport models are needed to evaluate the ability of the inversion
118 framework to assimilate such new observations.

119 In this study, we apply the chemistry transport model LMDzINCA (Folberth et al., 2006;
120 Hauglustaine et al., 2004; Hourdin et al., 2006; Szopa et al., 2013) zoomed down to a
121 horizontal resolution of ~50km over SEA to simulate the variations of CH₄ and CO₂ during
122 the period 2006–2013. The model performance is evaluated against observations from 39
123 global and regional stations inside and outside the zoomed region. The variability of the
124 observed or simulated concentrations at each station is decomposed for evaluation at different
125 temporal scales, namely: the annual mean gradients between stations, the seasonal cycle, the
126 synoptic variability and the diurnal cycle. For comparison, a non-zoomed standard version of
127 the same transport model is also run with the same set of surface fluxes and the same vertical
128 pressure levels, in order to estimate the improvement brought by the zoomed configuration.
129 The detailed description of the observations and the chemistry transport model is presented in
130 Section 2, together with the prescribed CH₄ and CO₂ surface fluxes that force the simulations,
131 as well as the metrics used to quantify the model performance. An evaluation of the
132 simulations performed is presented and discussed in Section 3, showing capabilities of the
133 transport model to represent the annual gradients between stations, and the seasonal, synoptic,
134 and diurnal variations. Conclusions and implications drawn from this study are given in
135 Section 4.

136 **2 Data and Methods**

137 **2.1 Model description**

138 2.1.1 LMDzINCA

139 The LMDzINCA model couples a general circulation model developed at the Laboratoire de
140 Météorologie Dynamique (LMD; Hourdin et al., 2006), and a global chemistry and aerosol
141 model INteractions between Chemistry and Aerosols (INCA; Folberth et al., 2006;
142 Hauglustaine et al., 2004). A more recent description of LMDzINCA is presented in Szopa et
143 al. (2013). To simulate CH₄ and CO₂ concentrations, we run a standard version of the model
144 with a horizontal resolution of 2.5° (i.e., 144 model grids) in longitude and 1.27° (i.e., 142
145 model grids) in latitude (hereafter this version is abbreviated as ‘STs’) and a zoomed version
146 with the same number of grid boxes, but a resolution of ~0.66° in longitude and ~0.51° in
147 latitude in a region of 50–130°E and 0–55°N centered over India and China (hereafter this
148 version is abbreviated as ‘ZAs’) (Figure 1; see also Wang et al., 2014, 2016). It means that, in

149 terms of the surface area, a gridcell from STs roughly contains 9 grid-cells from ZAs within
150 the zoomed region. Both model versions are run with 19 and 39 sigma-pressure layers, thus
151 rendering four combinations of horizontal and vertical resolutions (i.e., ST19, ZA19, ST39,
152 ZA39). Vertical diffusion and deep convection are parameterized following the schemes of
153 Louis (1979) and Tiedtke (1989), respectively. The simulated horizontal wind vectors (u and
154 v) are nudged towards the 6-hourly European Center for Medium Range Weather Forecast
155 (ECMWF) reanalysis dataset (ERA-I) in order to simulate the observed large scale advection
156 (Hourdin and Issartel, 2000).

157 The atmospheric concentrations of hydroxyl radicals (OH), the main sink of atmospheric CH₄,
158 are produced from a simulation at a horizontal resolution of 3.75° in longitude (i.e., 96 model
159 grids) and 1.9° in latitude (i.e., 95 model grids) with the full INCA tropospheric
160 photochemistry scheme (Folberth et al., 2006; Hauglustaine et al., 2004, 2014). The OH
161 fields are climatological monthly data, and are regridded to the standard and zoomed model
162 grids, respectively. It should be noted that the spatiotemporal distributions of the OH
163 concentrations have large uncertainties and vary greatly among different chemical transport
164 models, therefore the choice of the OH fields may affect the evaluation for CH₄ (especially in
165 terms of the annual gradients between stations and the seasonal cycles). In this study, as we
166 focus more on the improvement of performance gained from refinement of the model
167 resolution rather than model-observation misfits and model bias in CH₄ growth rates, the
168 influences of OH variations on model improvement are assumed to be very small given that
169 the OH fields for both ZAs and STs are regridded from a lower model resolution and thus
170 don't show much difference between the two model versions.

171 The CH₄ and CO₂ concentrations are simulated over the period 2000–2013 with both STs and
172 ZAs. The first six years (2000–2005) of the simulations are considered as model spin-up,
173 thus we only compared the simulated CH₄ and CO₂ concentrations with observations during
174 2006–2013. The initial CH₄ concentration field is defined based on the optimized initial state
175 from a CH₄ inversion that assimilates observations from 50+ global background stations over
176 the period 2006–2012 (Locatelli, 2014; Locatelli et al., 2015c). The optimized initial CH₄
177 concentration field for the year 2006 is rescaled to the levels of the year 2000 and used as the
178 initial state in our simulations.. The time step of model outputs is hourly.

179 2.1.2 Prescribed CH₄ and CO₂ surface fluxes

180 The prescribed CH₄ and CO₂ surface fluxes used as model inputs are presented in Table 1.
181 We simulate the CH₄ concentration fields using a combination of the following datasets: (1)
182 the interannually varying anthropogenic emissions obtained from the Emission Database for
183 Global Atmospheric Research (EDGAR) v4.2 FT2010 product (<http://edgar.jrc.ec.europa.eu>),
184 including emissions from rice cultivation with the seasonal variations based on Matthews et
185 al. (1991) imposed to the original yearly data; (2) climatological wetland emissions based on
186 the scheme developed by Kaplan et al. (2006); (3) interannually and seasonally varying
187 biomass burning emissions from Global Fire Emissions Database (GFED) v4.1 product
188 (Randerson et al., 2012; Van Der Werf et al., 2017; <http://www.globalfiredata.org/>), (4)
189 climatological termite emissions (Sanderson, 1996), (5) climatological ocean emissions
190 (Lambert and Schmidt, 1993), and (6) climatological soil uptake (Ridgwell et al., 1999). Note
191 that for anthropogenic emissions from sectors other than rice cultivation, **the seasonal**
192 **variations are much smaller, and monthly sector-specific dataset is currently not available for**
193 **the whole study period. Therefore we do not consider seasonal variations in CH₄ emissions**
194 **from those sectors.** Based on these emission fields, the global CH₄ emissions in 2010 are 550
195 TgCH₄/yr, and 194 TgCH₄/yr over the zoomed region. For the years over which CH₄
196 anthropogenic emissions (namely, the years 2011–2013) were not available from the data
197 sources when the simulations were performed, we use emissions for the year 2010.

198 The prescribed CO₂ fluxes used to simulate the concentration fields are based on the
199 following datasets: (1) three variants (hourly, daily, and monthly means) of interannually
200 varying fossil fuel emissions produced by the Institut für Energiewirtschaft und Rationelle
201 Energieanwendung (IER), Universität Stuttgart on the basis of EDGARv4.2 product
202 (hereafter IER-EDGAR, <http://carbones.ier.uni-stuttgart.de/wms/index.html>) (Pregger et al.,
203 2007); (2) interannually and seasonally varying biomass burning emission from GFEDv4.1
204 (Randerson et al., 2012; Van Der Werf et al., 2017; <http://www.globalfiredata.org/>); (3)
205 interannually and hourly varying terrestrial biospheric fluxes produced from outputs of the
206 Organizing Carbon and Hydrology in Dynamic Ecosystem (ORCHIDEE) model; and (4)
207 interannually and seasonally varying air-sea CO₂ gas exchange maps developed by NOAA's
208 Pacific Marine Environmental Laboratory (PMEL) and Atlantic Oceanographic and
209 Meteorological Laboratory (AOML) groups (Park et al., 2010). Here ORCHIDEE runs with
210 the trunk version r1882 (source code available at

211 <https://forge.ipsl.jussieu.fr/orchidee/browser/trunk#ORCHIDEE> with the revision number of
212 r1882), using the same simulation protocol as the SG3 simulation in MsTMIP project
213 (Huntzinger et al., 2013). The climate forcing data are obtained from CRUNCEP v5.3.2,
214 while the yearly land use maps, soil map and other forcing data (e.g., monthly CO₂
215 concentrations) are as described in Wei et al. (2014). The sum of global net CO₂ surface
216 fluxes in 2010 are 6.9 PgC/yr, and 3.9 PgC/yr over the zoomed region. For the CO₂ fossil fuel
217 emissions, the IER-EDGAR product is only available until 2009. To generate the emission
218 maps for the years 2010–2013, we scaled the emission spatial distribution in 2009 using the
219 global totals for these years based on the EDGARv4.2FT2010 datasets. The detailed
220 information for each surface flux is listed in Table 1.

221 **2.2 Atmospheric CH₄ and CO₂ observations**

222 The simulated CH₄ and CO₂ concentrations are evaluated against observations from 20 flask
223 and 13 continuous surface stations within and around the zoomed region (Figure 1), operated
224 by different programs and organizations (Table 2). The stations where flask observations are
225 published (12 stations) mainly belong to the cooperative program organized by the NOAA
226 Earth System Research Laboratory (NOAA/ESRL, available at
227 ftp://aftp.cmdl.noaa.gov/data/trace_gases/). We also use flask observations from stations
228 operated by China Meteorological Administration (CMA, China) (the JIN, LIN and LON
229 stations, see also Fang et al., 2014), Commonwealth Scientific and Research Organization
230 (CSIRO, Australia) (the CRI station, Bhattacharya et al., 2009, available at
231 <http://ds.data.jma.go.jp/gmd/wdcgg/>), Indian Institute of Tropical Meteorology (IITM, India)
232 (the SNG station, see also Tiwari et al., 2014), and stations from the Indo-French cooperative
233 research program (the HLE, PON and PBL stations, Lin et al., 2015; Swathi et al., 2013). All
234 the CH₄ (CO₂) flask measurements are reported on or linked to the NOAA2004
235 (WMOX2007) calibration scale, which guarantees comparability between stations in terms of
236 annual means.

237 The continuous CH₄ and CO₂ measurements are obtained from 13 stations operated by Korea
238 Meteorological Administration (KMA, Korea) (the AMY and GSN stations), Aichi Air
239 Environment Division (AAED, Japan) (the MKW station), Japan Meteorological Agency
240 (JMA) (the MNM, RYO and YON stations), National Institute for Environmental Studies
241 (NIES, Japan) (the COI and HAT stations), Agency for Meteorology, Climatology and

242 Geophysics (BMKG, Indonesia) and Swiss Federal Laboratoires for Materials Testing and
243 Research (Empa, Switzerland) (the BKT station). These datasets are available from the World
244 Data Center for Greenhouse Gases (WDCGG, <http://ds.data.jma.go.jp/gmd/wdogg/>). Besides,
245 continuous CH₄ and CO₂ measurements are also available from HLE and PON that have been
246 maintained by the Indo-French cooperative research program between LSCE in France and
247 IIA and CSIR4PI in India (Table 2). All the continuous CH₄ (CO₂) measurements used in this
248 study are reported on or traceable to the NOAA2004 (WMOX2007) scale except AMY, COI
249 and HAT. The CO₂ continuous measurements at COI are reported on the NIES95 scale,
250 which is 0.10 to 0.14 ppm lower than WMO in a range between 355 and 385 ppm (Machida
251 et al., 2009). The CH₄ continuous measurements at COI and HAT are reported on the NIES
252 scale, with a conversion factor to WMO scale of 0.9973 (JMA and WMO, 2014). For AMY,
253 the CH₄ measurements over most of the study period are reported on the KRISS scale but
254 they are not traceable to the WMO scale (JMA and WMO, 2014); therefore, we discarded
255 this station from the subsequent analyses of the CH₄ annual gradients between stations. Note
256 that most of the stations where continuous observations are available are located on the east
257 part of the zoomed region, with the exception of HLE, PON and BKT. The stations used in
258 this study span a large range of geographic locations (marine, coastal, mountain or
259 continental) with polluted and non-polluted environments. Both flask and continuous
260 measurements are used to evaluate the model's ability in representing the annual gradient
261 between stations, the seasonal cycle and the synoptic variability for CH₄ and CO₂. The
262 continuous measurements are also used to analyze the diurnal cycle for these two gases.

263 To evaluate the model performance with regards to vertical transport, we also use
264 observations of the CO₂ vertical profiles from passenger aircraft from the Comprehensive
265 Observation Network for TRace gases by AirLiner (CONTRAIL) project (Machida et al.,
266 2008, <http://www.cger.nies.go.jp/contrail/index.html>). This dataset provides high-frequency
267 CO₂ measurements made by on-board continuous CO₂ measuring equipments (CMEs) during
268 commercial flights between Japan and other Asian countries. The CONTRAIL data are
269 reported on the NIES95 scale, which is 0.10 to 0.14 ppm lower than WMO in a range
270 between 355 and 385 ppm (Machida et al., 2009). In this study, we select from the
271 CONTRAIL dataset all the CO₂ vertical profiles over SEA during the ascending and
272 descending flights for the period 2006–2011, which provided 1808 vertical profiles over a
273 total of 32 airports (Figure S1 and S2).

274 **2.3 Sampling methods and data processing**

275 The model outputs are sampled at the nearest gridpoint and vertical level to each station for
276 both STs and ZAs. For flask stations, the model outputs are extracted at the exact hour when
277 each flask sample was taken. For continuous stations below 1000 m.a.s.l., since both STs and
278 ZAs cannot reproduce accurately the nighttime CH₄ and CO₂ accumulation near the ground
279 as in most transport models (Geels et al., 2007), only afternoon (12:00–15:00 LST) data are
280 retained for further analyses of the annual gradients, the seasonal cycle and the synoptic
281 variability. For continuous stations above 1000 m.a.s.l. (only HLE in this study), nighttime
282 (00:00–3:00 LST) data are retained, to avoid sampling local air masses advected by upslope
283 winds from nearby valleys. During daytime, the local valley ascendances and the complex
284 terrain mesoscale circulations cannot be captured by a global transport model.

285 The curve-fitting routine (CCGvu) developed by NOAA Climate Monitoring and Diagnostic
286 Laboratory (NOAA/CMDL) is applied to the modelled and observed CH₄ and CO₂ time
287 series to extract the annual means, monthly smoothed seasonal cycles and synoptic variations
288 (Thoning et al., 1989). For each station, a smoothed function is fitted to the observed or
289 modelled time series, which consists of a first-order polynomial for the growth rate, two
290 harmonics for the annual cycle (Levin et al., 2002; Ramonet et al., 2002), and a low-pass
291 filter with 80 and 667 days as short-term and long-term cutoff values, respectively (Bakwin et
292 al., 1998). The annual means and the mean seasonal cycle are calculated from the smoothed
293 curve and harmonics, while the synoptic variations are defined as the residuals between the
294 original data and the smoothed fitting curve. Note that we have excluded the observations
295 lying beyond three standard deviations of the residuals around the fitting curve, which are
296 likely to be outliers that are influenced by local fluxes. More detailed descriptions about the
297 curve-fitting procedures and the set-up of parameters can be found in Section 2.3 of Lin et al.
298 (2015).

299 For the CO₂ vertical profiles from the CONTRAIL passenger aircraft programme, since CO₂
300 data have been continuously taken every 10 seconds by the onboard CMEs, we average the
301 observed and corresponding simulated CO₂ time series into altitude bins of 1km from the
302 surface to the upper troposphere. We also divide the whole study area into four major
303 subregions for which we group all available CONTRAIL CO₂ profiles (Figure S1), namely
304 East Asia (EAS), the Indian sub-continent (IND), Northern Southeast Asia (NSA) and

305 Southern Southeast Asia (SSA). Given that there are model-observation discrepancies in CO₂
306 growth rates as well as misfits of absolute CO₂ concentrations, the observed and simulated
307 CONTRAIL time series have been detrended before comparisons of the vertical gradients. To
308 this end, over each subregion, we detrend for each altitude bin the observed and simulated
309 CO₂ time series, by applying the respective linear trend fit to the observed and simulated CO₂
310 time series of the altitude bin 3–4 km. This altitude bin is thus chosen as reference due to
311 greater data availability compared to other altitudes, and because this level is outside the
312 boundary layer where aircraft CO₂ data are more variable and influenced by local sources
313 (e.g. airports and nearby cities). The detrended CO₂ (denoted as ΔCO_2) referenced to the 3-4
314 km altitude are seasonally averaged for each altitude bin and each subregion, and the
315 resulting vertical profiles of ΔCO_2 are compared between simulations and observations.

316 **2.4 Metrics**

317 In order to evaluate the model performance to represent observations at different time scales
318 (annual, seasonal, synoptic, diurnal), following Cadule et al. (2010), we define a series of
319 metrics and corresponding statistics for each time scale. All the metrics, defined below, are
320 calculated for both observed and simulated CH₄ (CO₂) time series between 2006 and 2013.

321 2.4.1 Annual gradients between stations

322 As inversions use gradients to optimize surface fluxes, it is important to have a metric based
323 upon cross-site gradients. We take Hanle in India (HLE – 78.96°N, 32.78°E, 4517 m a.s.l.,
324 Figure 1, Table 2) as a reference and calculate the mean annual gradients by subtracting CH₄
325 (CO₂) at HLE from those of other stations. HLE is a remote station in the free troposphere
326 within SEA and is located far from any important source/sink areas for both CH₄ and CO₂.
327 These characteristics make HLE an appropriate reference to calculate the gradients between
328 stations. Concentration gradients to HLE are calculated for both observations and model
329 simulations using the corresponding smoothed curves fitted with the CCGvu routine (see
330 Section 2.3). The ability of ZAs and STs to represent the observed CH₄ (CO₂) annual
331 gradients across all the available stations is quantified by the mean bias (MB, Eq. 1) and the
332 root-mean-square deviation (RMSE, Eq. 2). In Eq. 1 and Eq. 2, m_i and o_i indicate
333 respectively the modelled and observed CH₄ (CO₂) mean annual gradient relative to HLE for
334 a station i .

335
$$MB = \frac{\sum_{i=1}^N (m_i - o_i)}{N} \quad (1)$$

336
$$RMSE = \sqrt{\frac{\sum_{i=1}^N (m_i - o_i)^2}{N}} \quad (2)$$

337 2.4.2 Seasonal cycle

338 Two metrics of the model ability to reproduce the observed CH₄ (CO₂) seasonal cycle are
 339 considered, the phase and the amplitude. For each station, the seasonal phase is evaluated by
 340 the Pearson correlation between the observed and simulated harmonics extracted from the
 341 original time series, whereas the seasonal cycle amplitude is evaluated by the ratio of the
 342 modelled to the observed seasonal peak-to-peak amplitudes based on the harmonics (A_m/A_o).

343 2.4.3 Synoptic variability

344 For each station, the performance of ZAs and STs to represent the phase (timing) of the
 345 synoptic variability is evaluated by the Pearson correlation coefficient between the modelled
 346 and observed synoptic deviations (residuals) around the corresponding smoothed fitting curve
 347 (see Section 2.3), whereas the performance for the amplitude of the synoptic variability is
 348 quantified by the ratio of standard deviations of the residual concentration variability between
 349 the model and observations (i.e., Normalized Standard Deviation, NSD, Eq. 3). Further, the
 350 overall ability of a model to represent the synoptic variability of CH₄ (CO₂) at a station is
 351 quantified by the RMSE (Eq. 4), a metric that can be represented with the Pearson correlation
 352 and the NSD in a Taylor diagram (Taylor, 2001). In Eq. 3 and Eq. 4, m_j (o_j) indicates the
 353 modelled (observed) synoptic event j , whereas \bar{m} (\bar{o}) indicates the arithmetic mean of all the
 354 modelled (observed) synoptic events over the study period. Note that for the flask
 355 measurements, j corresponds to the time when a flask sample was taken, whereas for the
 356 continuous measurements, j corresponds to the early morning (00:00–03:00LST, for
 357 mountain stations) or afternoon (12:00–15:00LST, for coastal or island stations) period of
 358 each sampling day.

359
$$NSD = \frac{\sqrt{\frac{\sum_{j=1}^N (m_j - \bar{m})^2}{N}}}{\sqrt{\frac{\sum_{j=1}^N (o_j - \bar{o})^2}{N}}} \quad (3)$$

360
$$RMSE = \sqrt{\frac{\sum_{j=1}^N (m_j - o_j)^2}{N}} \quad (4)$$

361 **2.4.4 Diurnal cycle**

362 For each station, the model's ability to reproduce the mean CH₄ (CO₂) diurnal cycle phase in
 363 a month is evaluated by the correlation of the hourly mean composite modelled and observed
 364 values, whereas model performance on the diurnal cycle amplitude is evaluated by the ratio
 365 of the modelled to the observed peak-to-peak amplitudes (A_m/A_o). For each station, daily
 366 means are subtracted from the raw data to remove any influence of interannual, seasonal or
 367 even synoptic variations.

368 **3 Results and discussions**

369 **3.1 Annual gradients**

370 **3.1.1 CH₄ annual gradients**

371 The annual mean gradient between a station and the HLE reference station relates to the time
 372 integral of transport of sources/sinks within the regional footprint area of the station on top of
 373 the background gradient caused by remote sources. For CH₄, Figure 2a,b shows the
 374 scatterplot of the simulated and observed mean annual gradients to HLE for all stations. In
 375 general, all the four model versions capture the observed CH₄ gradients with reference to
 376 HLE, and the simulated gradients roughly distribute around the identity line (Figure 2a,b).
 377 Compared to standard versions (STs), the zoom versions (ZAs) better represent the CH₄
 378 gradients for stations within the zoomed region (closed circles in Figure 2a,b), with RMSE
 379 decreasing by 20% and 16% for 19- and 39-layer models (Figure 2a,b and Table S1a). Note
 380 that increasing vertical resolution does not much impact the overall model performance, but
 381 the combination with the zoomed grid (i.e. ZA39) may inflate the model-observation misfits
 382 at a few stations with strong sources nearby (e.g. TAP and UUM in Table S2a). The better

383 performance of ZAs within the zoomed region is also found for different seasons (Figure S3).
384 Outside the zoomed region (open circles in Figure 2a,b), the performance of ZAs does not
385 significantly deteriorate despite the coarser resolution.

386 When looking into the model performance for different station types, ZAs generally better
387 capture the gradients at coastal and continental stations within the zoomed region, given the
388 substantial reduction of RMSE compared to STs (Table S1). For example, significant model
389 improvement is found at Shangdianzi (SDZ – 117.12°E, 40.65°N, 293m a.s.l.) and
390 Pondicherry (PON – 79.86°E, 12.01°N, 30m a.s.l.) (Figure 2a,b), each having an average bias
391 reduction of 28.1 (73.0%) and 30.3 (94.7%) ppb respectively compared to STs for the 39-
392 layer model (Table S2). This improvement mainly results from reduction in representation
393 error with higher model horizontal resolutions in the zoomed region, through better
394 description of surface fluxes and/or transport around the stations. Particularly, given the
395 presence of large CH₄ emission hotspots within the zoomed region (Figure S4), ZAs makes
396 the simulated CH₄ fields more heterogeneous around emission hotspots (e.g., North China in
397 Figure S5), having the potential to better represent stations nearby on an annual basis if the
398 surface fluxes are prescribed with sufficient accuracy (see Figure S6 for SDZ).

399 However, finer resolutions may enhance model-data misfits due to inaccurate meteorological
400 forcings and/or surface flux maps. For example, for the coastal station Tae-ahn Peninsula
401 (TAP – 126.13°E, 36.73°N, 21m a.s.l.) with significant emission sources nearby (Figure S6),
402 both ZAs and STs overestimate the observed CH₄ gradients by > +15 ppb, and ZA39 perform
403 even worse than other versions (Table S2). The poor model performance at TAP suggests that
404 the prescribed emission sources are probably overestimated within the station's footprint area
405 (also see the marine station GSN, Figure S6), and higher model resolutions (whether in
406 horizontal or in vertical) tend to inflate the model-observation misfits in this case. Besides, as
407 stated in several previous studies (Geels et al., 2007; Law et al., 2008; Patra et al., 2008), for
408 a station located in a complex terrain (e.g. coastal or mountain sites), the selection of an
409 appropriate gridpoint and/or model level to represent an observation is challenging. In this
410 study we sample the gridpoint and model level nearest to the location of the station, which
411 may not be the best representation of data sampling selection strategy (e.g. marine sector at
412 coastal stations or strong winds) and could contribute to the model-observation misfits.

413 3.1.2 CO₂ annual gradients

414 Both ZAs and STs can generally capture the CO₂ annual gradients between stations, although
415 not as well as for CH₄ (Figure 2c,d). In contrast with CH₄, ZAs does not significantly
416 improve representation of CO₂ gradients for stations within the zoomed region, with the mean
417 bias and RMSE close to those of STs (Table S1b). At a few stations (e.g., TAP), ZAs even
418 degrade model performance (Figure S8, Table S2b), possibly related to misrepresentation of
419 CO₂ sources in the prescribed surface fluxes and transport effects. Again increasing model
420 vertical resolution does not much impact the overall model performance.

421 With finer horizontal resolution, the model improvement to represent the annual gradients is
422 more apparent for CH₄ than for CO₂. One of the reasons may point towards the quality of
423 CO₂ surface fluxes, especially natural ones. They are spatially more diffuse than those of CH₄,
424 and temporally more variable in response to weather changes (Parazoo et al., 2008; Wang et
425 al., 2007). Therefore, the regional variations of net ecosystem exchange (NEE) not captured
426 by the terrestrial ecosystem model (e.g. ORCHIDEE in this paper) may explain the worse
427 model performance on the CO₂ annual gradients compared to CH₄, and less apparent model
428 improvement. Further, the spatial resolution of the prescribed surface flux may also account
429 for the difference in model improvement between CO₂ and CH₄ (e.g. the spatial resolution of
430 anthropogenic emissions is 1° for CO₂ and 0.1° for CH₄). Therefore, with current setup of
431 surface fluxes (Table 1), ZAs is more likely to resolve the spatial heterogeneity of CH₄ fields,
432 and its improvement over STs is more apparent than that for CO₂.

433 3.2 Seasonal cycles

434 3.2.1 CH₄ seasonal cycles

435 The model performance for the seasonal cycle depends on quality of seasonal surface fluxes,
436 atmospheric transport, and chemistry (for CH₄ only). For CH₄, both ZAs and STs very well
437 capture the seasonal phases at most stations within the zoomed region (Figure 3a), and model
438 resolutions (in both horizontal and vertical) do not significantly impact the simulated timing
439 of seasonal maximum and minimum. The seasonal phases at Plateau Assy (KZM – 77.87°E,
440 43.25°N, 2524m a.s.l.), Waliguan (WLG – 100.90°E, 36.28°N, 3890m a.s.l.) and Ulaan Uul
441 (UUM – 111.10°E, 44.45°N, 1012m a.s.l.) are not well represented, probably related to
442 unresolved seasonally varying sources around these stations. The sensitivity test simulations

443 prescribed with wetland emissions from ORCHIDEE outputs show much better model-
444 observation agreement in seasonal phases (Figure S9). For stations outside the zoomed region,
445 the performance of ZAs is not degraded despite the coarser horizontal resolutions (Figure
446 S10).

447 With respect to the seasonal amplitude, the performance of STs and ZAs shows significant
448 difference at stations influenced by large emission sources. For example, the seasonal
449 amplitudes of AMY and TAP are strongly overestimated by STs ($A_m/A_o=2.99$ and
450 $A_m/A_o=5.11$ for the 39-layer model; Figure 3a), while ZAs substantially decrease the
451 simulated amplitudes at these two stations with improved model-observation agreement
452 ($A_m/A_o=2.24$ and $A_m/A_o=2.80$ for the 39-layer model; Figure 3a). However, at SDZ the
453 seasonal amplitude is even more exaggerated by ZAs, especially when higher vertical
454 resolution is applied ($A_m/A_o=1.70$ and $A_m/A_o=2.03$ for ST39 and ZA39; Figure 3a). The two
455 contrasting cases suggest that increasing horizontal resolution does not necessarily better
456 represent CH₄ seasonal cycle, and model improvement/degradation depends on other factors
457 such as accuracy of the temporal and spatial variations of prescribed fluxes, OH fields and
458 meteorological forcings. Besides, as it is found for annual CH₄ gradients, we note that the
459 simulated seasonal amplitudes at stations in East Asia (AMY, TAP, GSN and SDZ) are
460 consistently higher than the observed ones (Figure 3a), implying that the prescribed CH₄
461 emissions are probably overestimated in this region.

462 3.2.2 CO₂ seasonal cycles

463 The CO₂ seasonal cycle mainly represents the seasonal cycle of NEE from ORCHIDEE
464 convoluted with atmospheric transport. Figure 3b illustrates that both ZAs and STs well
465 capture the CO₂ seasonal phases at most stations, and a high correlation (Pearson correlation
466 $R>0.8$) between the simulated and observed CO₂ harmonics is found for 14 out of 20 stations
467 within the zoomed region. However, the simulated onset of CO₂ uptake in spring or timing of
468 the seasonal minima tend to be earlier than observations. This shift in phase can be as large
469 as >1 month for several stations (e.g. HLE, JIN and PON in Figure 3b), yet cannot be reduced
470 by solely refining model resolutions. At BKT in western Indonesia, the shape of the CO₂

471 seasonality is not well captured ($R=0.27$ and $R=0.30$ for ST39 and ZA39; Figure 3b). Given
472 that representation of the CH_4 seasonal phase at BKT is very good ($R=0.97$ for ST39 and
473 ZA39; Figure 3a), the unsatisfactory model performance for CO_2 suggests inaccurate
474 seasonal variations in the prescribed surface fluxes such as NEE and/or fire emissions. As for
475 CH_4 , the performance of ZAs is not degraded outside the zoomed region despite the coarser
476 horizontal resolutions (Figure S11).

477 With respect to the CO_2 seasonal amplitude, 10 out of 20 stations within the zoomed region
478 are underestimated by more than 20%, most of which are mountain and continental stations
479 (Figure 3b). The underestimation of CO_2 seasonal amplitudes at these stations is probably due
480 to the underestimated carbon uptake in northern mid-latitudes by ORCHIDEE, which is the
481 case for most land surface models currently available (Peng et al., 2015). Another reason may
482 be related to the misrepresentation of CO_2 seasonal rectifier effect (Denning et al., 1995),
483 which means that the covariance between carbon exchange (through photosynthesis and
484 respiration) and vertical mixing may not be well captured in our simulations even with finer
485 model resolutions.

486 **3.3 Synoptic variability**

487 3.3.1 CH_4 synoptic variability

488 The day-to-day variability of CH_4 and CO_2 residuals are influenced by the regional
489 distribution of fluxes and atmospheric transport at the synoptic scale. For CH_4 , as shown in
490 Figure 4a, both STs and ZAs fairly well capture the phases of synoptic variability at most
491 stations within the zoomed region, with 15 out of 18 stations showing model-observation
492 correlation $r>0.3$. Increasing horizontal resolution can more or less impact model
493 performance, yet the direction of change is station-dependent. In general, ZAs improve
494 correlation in phases for most marine and coastal stations compared to STs (e.g., CRI and
495 HAT; Figure 4a), while degradation in model performance is mostly found for mountain and
496 continental stations (e.g. KZM and SDZ; Figure 4a). With increased horizontal resolution,
497 better characterization of the phases would require accurate representation of short-term
498 variability in both meteorological forcings and emission sources at fine scales. This presents
499 great challenges on data quality of boundary conditions, especially for mountain stations
500 located in complex terrains or continental stations surrounded by highly heterogeneous yet
501 uncertain emission sources.

502 Regarding the amplitudes of CH₄ synoptic variability, 12 out of 18 stations have NSDs within
503 the range of 0.6–1.5, and ZAs generally give higher NSD values than STs for most of these
504 stations (Figure 4b). For stations with NSDs>1.5, ZAs tend to simulate smaller amplitudes
505 and slightly improve model performance (e.g., GSN, HLE and SDZ; Figure 4b). One
506 exception is UUM. Given the presence of a wrong emission hotspot near the station in the
507 EDGARv4.2FT2010 dataset, ZAs greatly inflate the model-observation misfits (Figure S13).
508 The sensitivity test simulations prescribed with an improved data version EDGARv4.3.2
509 show much better agreement with observations, although the simulated amplitudes are still
510 too high. Besides, it is interesting to note that stations in East Asia generally have NSDs>1.5
511 (e.g., GSN, TAP, SDZ, and UUM; Figure 4b), again suggesting overestimation of the
512 prescribed CH₄ emissions in this region.

513 3.3.2 CO₂ synoptic variability

514 For CO₂, as shown in Figure 4c and 4d, 12 out of 20 stations within the zoomed region have
515 model-observation correlation $r>0.3$, whereas 14 out of 20 stations have NSDs within the
516 range of 0.5–1.5. With finer model resolution, significant model improvement (whether
517 regarding phases or amplitudes of CO₂ synoptic variability) is mostly found at marine, coastal
518 and continental stations (e.g., AMY, DSI, and SDZ; Figure 4c,d); for mountain stations, on
519 the contrary, phase correlation is not improved and representation of amplitudes is even
520 degraded (e.g. HLE, LLN and WLG; Figure 4c,d). As mentioned above for CH₄ synoptic
521 variability, the model degradation at mountain stations may arise from errors in mesoscale
522 meteorology and regional distribution of sources/sinks over complex terrains, probably as
523 well as unresolved vertical processes.

524 When we examine model performance for CO₂ versus CH₄ by stations, there are stations at
525 which phases of synoptic variability are satisfactorily captured for CH₄ but not for CO₂ (e.g.,
526 BKT, PBL, PON; Figure 4a,c). At PON, a tropical station on the southeast coast of India, the
527 simulated CO₂ synoptic variability is even out of phase with observations all year around and
528 during different seasons (Figure S14; Table S3). The poor model performance should be
529 largely attributed to the imperfect prescribed CO₂ surface fluxes. As noted by several
530 previous studies (e.g., Patra et al., 2008), CO₂ fluxes with sufficient accuracy and resolution
531 are indispensable for realistic simulation of CO₂ synoptic variability. In this study, the daily
532 to hourly NEE variability does not seem to be well represented in ORCHIDEE, especially in

533 the tropics. Further, for stations influenced by large fire emissions (e.g., BKT), using the
534 monthly averaged biomass burning emissions may not be able to realistically simulate CO₂
535 synoptic variability due to episodic biomass burning events. Besides, the prescribed CO₂
536 ocean fluxes have a rather coarse spatial resolution (4°×5°), which may additionally account
537 for the poor model performance, especially for marine and coastal stations.

538 **3.4 Diurnal cycle**

539 3.4.1 CH₄ diurnal cycle

540 The diurnal cycles of trace gases are mainly controlled by the co-variations between local
541 surface fluxes and atmospheric transport. To illustrate model performance on diurnal cycles,
542 we take a few stations with continuous measurements as examples. For CH₄, as shown in
543 Figure 5a, the mean diurnal cycles can be reasonably well represented at the marine/coastal
544 stations GSN and PON for the specific study periods (also see Table S4), although monthly
545 fluxes are used to prescribe the models. Compared to STs, the diurnal cycles simulated by
546 ZAs agree much better with observations (Figure 5a), possibly due to more realistic
547 representation of coastal topography, land-sea breeze, and/or source distribution at finer grids.
548 However, there are also periods during which the CH₄ diurnal cycles are not satisfactorily
549 represented by both model versions, or model performance is degraded with higher
550 horizontal/vertical resolutions (Table S4). The model-observation mismatch may be
551 explained by the following reasons. First, the prescribed monthly surface fluxes are probably
552 not adequate to resolve the short-term variability at stations strongly influenced by local and
553 regional sources, especially during the seasons when emissions from wetlands and rice
554 paddies are active and temporally variable with temperature and moisture. Second, the sub-
555 grid scale parameterizations in the current model we used are not able to realistically simulate
556 the diurnal cycles of boundary layer mixing. Recently [new physical parameterizations have
557 been implemented in LMDz to better simulate vertical diffusion and mesoscale mixing by
558 thermal plumes in the boundary layer \(Hourdin et al., 2002; Rio et al., 2008\), which can
559 significantly improve simulation of the daily peak values during nighttime and thus diurnal
560 cycles of tracer concentrations \(Locatelli et al., 2015b\).](#)

561 Representation of the CH₄ diurnal cycle at mountain stations can be even more complicated,
562 given that the mesoscale atmospheric transports such as mountain-valley circulations and
563 terrain-induced up-down slope circulations cannot be resolved in global transport models

564 (Griffiths et al., 2014; Pérez-Landa et al., 2007; Pillai et al., 2011). At BKT, a mountain
565 station located on an altitude of 869 m a.s.l., the CH₄ diurnal cycle is not reasonably
566 represented when model outputs are sampled at the levels corresponding to this altitude (Level
567 3 and Level 4 for 19-layer and 39-layer models). The simulated CH₄ diurnal cycles sampled
568 at a lower model level (Level 2 for both 19-layer and 39-layer models) agree much better
569 with the observed ones (Figure 5a). This suggests that the current model in use is not able to
570 resolve mesoscale circulations in complex terrains, even with the zoomed grids (~50 km over
571 the focal area) and 39 model layers.

572 3.4.2 CO₂ diurnal cycle

573 For CO₂, as shown in Figure 5b, the simulated diurnal cycles at GSN and PON correlate
574 fairly well with the observed ones for their specific study periods (also see Table S5). The
575 amplitudes of diurnal cycles are greatly underestimated, although this can be more or less
576 improved with finer horizontal resolutions (Figure 5b). As for CH₄, the model-observation
577 discrepancies mainly result from underestimated NEE diurnal cycles from ORCHIDEE
578 and/or unresolved processes in the planetary boundary layer. Particularly, neither ZAs nor
579 STs are able to adequately capture the CO₂ diurnal rectifier effect (Denning et al., 1996). For
580 stations strongly influenced by local fossil fuel emissions, underestimation of the amplitudes
581 may be additionally attributed to fine-scale sources not resolved at current horizontal
582 resolutions. This is the case for PON, a coastal station 8 km north of the city of Pondicherry
583 in India with a population of around 750,000 (Lin et al., 2015), where the amplitudes of
584 diurnal cycles are underestimated for both CO₂ and CH₄ (Figure 5a,b). Again at BKT, as
585 noted for CH₄, a better model-observation agreement is found for the CO₂ diurnal cycle when
586 model outputs are sampled at the surface layer rather than the one corresponding to the
587 station altitude (Figure 5b). Note that even the simulated diurnal cycles at the surface level
588 are smaller compared to the observed ones by ~50%, suggesting that the diurnal variations of
589 both NEE fluxes and terrain-induced circulations are probably not satisfactorily represented
590 in the current simulations.

591 3.5 Evaluation against the CONTRAIL CO₂ vertical profiles

592 Figure 6 shows the simulated and observed CO₂ vertical profiles averaged for different
593 seasons and over different regions. Over East Asia (EAS; Figure 6a and Figure S1), both ZAs
594 and STs reasonably reproduce the shape of the observed CO₂ vertical profiles above 2 km,

595 while below 2 km the magnitude of ΔCO_2 is significantly underestimated by up to 5 ppm.
596 The simulated CO_2 vertical gradients between planetary boundary layer (BL) and free
597 troposphere (FT) are lower than the observations by 2–3 ppm during winter (Figure 7a). The
598 model-observation discrepancies are possibly due to stronger vertical mixing in LMDz
599 (Locatelli et al., 2015a; Patra et al., 2011) as well as flux uncertainty. Note that as most
600 samples (79%) are taken over the Narita International Airport (NRT) and Chubu Centrair
601 International Airport (NGO) in Japan located outside the zoomed region (Figure S1), STs
602 slightly better capture the BL-FT gradients than ZAs.

603 Over the Indian sub-continent (IND, Figure 6b), there is large underestimation of the
604 magnitude of ΔCO_2 near the surface by up to 8 ppm during April–June (AMJ), July–
605 September (JAS) and October–December (OND). Accordingly, the BL-FT gradients are also
606 underestimated by up to 3–4ppm for these periods (Figure 7b). The model-observation
607 discrepancies are probably due to vertical mixing processes not realistically simulated in the
608 current model (including deep convection), as well as the imperfect representation of CO_2
609 surface fluxes strongly influenced by the Indian monsoon system.

610 The CO_2 vertical profiles over Southeast Asia (including Northern Southeast Asia (NSA) and
611 Southern Southeast Asia (SSA)) are generally well reproduced (Figure 6c,d). However, both
612 ZAs and STs fail to reproduce the BL-FT gradient of ~ 3 ppm in April for NSA (Figure 7c).
613 Apart from errors due to vertical transport and/or prescribed NEE, inaccurate estimates of
614 biomass burning emissions could also contribute to this model-observation mismatch.

615 Overall, the CO_2 vertical profiles in free troposphere are well simulated by both STs and ZAs
616 over SEA, while significant underestimation of the BL-FT gradients is found for East Asia
617 and the Indian sub-continent. The model-observation mismatch is due to misrepresentation of
618 both vertical transport and prescribed surface fluxes, and can not be significantly reduced by
619 solely refining the horizontal/vertical resolution, as shown by the very similar CO_2 vertical
620 profiles simulated from ZAs and STs. New physical parameterization as shown in Locatelli et
621 al., (2015a) should be implemented in the model to assess its potential to improve simulation
622 of the vertical profiles of trace gases (especially the BL-FT gradients).

623 **4 Conclusions and implications**

624 In this study, we assess the capability of a global transport model (LMDzINCA) to simulate
625 CH₄ and CO₂ variabilities over South and East Asia (SEA). Simulations have been performed
626 with configurations of different horizontal (standard (STs) versus Asian zoom (ZAs)) and
627 vertical (19 versus 39) resolutions. Model performance to represent trace gas variabilities is
628 evaluated for each model version at multi-annual, seasonal, synoptic and diurnal scales,
629 against flask and continuous measurements from a unique dataset of 39 global and regional
630 stations inside and outside the zoomed region. The evaluation at multiple temporal scales and
631 comparisons between different model resolutions and trace gases have informed us of both
632 advantages and challenges relating to high resolution transport modelling. Main conclusions
633 and implications for possible model improvement and inverse modeling are summarized as
634 follows.

635 First, ZAs improve the overall representation of CH₄ annual gradients between stations in
636 SEA, with reduction of RMSE by 16–20% compared to STs. The model improvement mainly
637 results from reduction in representation error with finer horizontal resolutions over SEA,
638 through better characterization of CH₄ surface fluxes, transport, and/or topography around
639 stations. Particularly, the scatterly distributed CH₄ emission sources (especially emission
640 hotspots) can be more precisely defined with the Asian zoom grids, which makes the
641 simulated concentration fields more heterogeneous, having the potential to improve
642 representation of stations nearby on an annual basis.

643 However, as the model resolution increases, the simulated CH₄ concentration fields are more
644 sensitive to possible errors in boundary conditions. Thus the performance of ZAs at a specific
645 station as compared to STs depends on the accuracy and data quality of meteorological
646 forcings and/or surface fluxes, especially when we examine short-term variabilities (synoptic
647 and diurnal variations) or stations influenced by significant emission sources around. One
648 example is UUM, at which ZAs even greatly degrade representation of synoptic variability
649 due to presence of a wrong emission hotspot near the station in the EDGARv4.2FT2010
650 dataset. A sensitivity test prescribed with the improved emission dataset EDGARv4.3.2 show
651 much better agreement with observations. This emphasizes importance of accurate a priori
652 CH₄ surface fluxes in high resolution transport modelling and inversions, particularly
653 regarding locations and magnitudes of emission hotspots. Any unrealistic emission hotspot

654 close to a station (as shown for UUM) should be corrected before inversions, otherwise the
655 inverted surface fluxes are likely to be strongly biased. Moreover, as current bottom-up
656 estimates of CH₄ sources and sinks still suffer from large uncertainties at fine scales, caution
657 should be taken when one attempts to assimilate observations not realistically simulated by
658 the high resolution transport model. These observations should be either removed from
659 inversions or allocated with large uncertainties.

660 With respect to CO₂, model performance and the limited model improvement with finer grids
661 suggest that the CO₂ surface fluxes have not been prescribed with sufficient accuracy and
662 resolution. One major component is NEE simulated from the terrestrial ecosystem model
663 ORCHIDEE. For example, the smaller CO₂ seasonal amplitudes simulated at most inland
664 stations in SEA mainly result from underestimated carbon uptake in northern mid-latitudes by
665 ORCHIDEE, while the misrepresentation of synoptic and diurnal variabilities (especially for
666 tropical stations like BKT and PON) is related to the inability of ORCHIDEE to satisfactorily
667 capture sub-monthly to daily profiles of NEE. More efforts should be made to improve
668 simulation of carbon exchange between land surface and atmosphere at various spatial and
669 temporal scales.

670 Furthermore, apart from data quality of the prescribed surface fluxes, representation of the
671 CH₄ and CO₂ short-term variabilities is also limited by model's ability to simulate boundary
672 layer mixing and mesoscale transport in complex terrains. The recent implementation of new
673 sub-grid physical parameterizations in LMDz is able to significantly improve simulation of
674 the daily maximum during nighttime and thus diurnal cycles of tracer concentrations
675 (Locatelli et al., 2015b). To fully take advantage of high-frequency CH₄ or CO₂ observations
676 at stations close to source regions, it is highly recommended to implement the new boundary
677 layer physics in the current transport model, in addition to refinement of model horizontal
678 and vertical resolutions. [The current transport model with old planetary boundary physics is
679 not capable to capture diurnal variations at continental or mountain stations, therefore only
680 observations that are well represented should be selected and kept for inversions \(e.g.
681 afternoon measurements for continental stations and nighttime measurements for mountain
682 stations\).](#)

683 Lastly, the model-observation comparisons at multiple temporal scales can give us
684 information about the magnitude of sources and sinks in the studied region. For example, at

685 GSN, TAP and SDZ, all of which located in East and Northeast Asia, the CH₄ annual
686 gradients as well as the amplitudes of seasonal and synoptic variability are consistently
687 overestimated, suggesting overestimation of CH₄ emissions in East Asia. Therefore
688 atmospheric inversions that assimilate information from these stations are expected to
689 decrease emissions in East Asia, which agree with several recent global or regional studies
690 from independent inventories (e.g., Peng et al., 2016) or inverse modeling (Bergamaschi et al.,
691 2013; Bruhwiler et al., 2014; Thompson et al., 2015). Further studies are needed in the future
692 to estimate CH₄ budgets in SEA by utilizing high resolution transport models that are capable
693 to represent regional networks of atmospheric observations.

694 **Acknowledgement**

695 This study was initiated within the framework of CaFICA-CEFIPRA project (2809-1). X. Lin
696 acknowledges the PhD funding support from AIRBUS Defense & Space. P. Ciais thanks the
697 ERC SyG project IMBALANCE-P ‘Effects of Phosphorus Limitations on Life, Earth System
698 and Society’ Grant agreement (no. 610028). N. Evangeliou acknowledges the Nordic Center
699 of Excellence eSTICC project (eScience Tools for Investigating Climate Change in northern
700 high latitudes) funded by Nordforsk (no. 57001). We acknowledge the WDCGG for
701 providing the archives of surface station observations for CO₂ and CH₄. We thank the
702 following networks or institutes for the efforts on surface GHG measurements and their
703 access: NOAA/ESRL, Aichi, BMKG, CMA, CSIR4PI, CSIRO, Empa, ESSO/NIOT, IIA,
704 IITM, JMA, KMA, LSCE, NIER, NIES, PU and Saitama. We also thank Dr. T. Machida
705 from NIES for providing CO₂ measurements from the CONTRAIL project. Finally, we
706 would like to thank F. Marabelle and his team at LSCE, and the CURIE (TGCC) platform for
707 the computing support.

708

709 **References**

- 710 Aalto, T., Hatakka, J., Karstens, U., Aurela, M., Thum, T. and Lohila, A.: Modeling
711 atmospheric CO₂ concentration profiles and fluxes above sloping terrain at a boreal site,
712 *Atmos. Chem. Phys.*, 6(2), 303–314, doi:10.5194/acp-6-303-2006, 2006.
- 713 Aalto, T., Hatakka, J. and Lallo, M.: Tropospheric methane in northern Finland: seasonal
714 variations, transport patterns and correlations with other trace gases, *Tellus B*, 59(2), 251–259,
715 doi:10.1111/j.1600-0889.2007.00248.x, 2007.
- 716 Bakwin, P. S., Tans, P. P., Hurst, D. F. and Zhao, C.: Measurements of carbon dioxide on
717 very tall towers: results of the NOAA/CMDL program, *Tellus B*, 50(5), 401–415,
718 doi:10.1034/j.1600-0889.1998.t01-4-00001.x, 1998.
- 719 Berchet, A., Pison, I., Chevallier, F., Paris, J.-D., Bousquet, P., Bonne, J.-L., Arshinov, M. Y.,
720 Belan, B. D., Cressot, C., Davydov, D. K., Dlugokencky, E. J., Fofonov, A. V., Galanin, A.,
721 Lavrič, J., Machida, T., Parker, R., Sasakawa, M., Spahni, R., Stocker, B. D. and Winderlich,
722 J.: Natural and anthropogenic methane fluxes in Eurasia: a mesoscale quantification by
723 generalized atmospheric inversion, *Biogeosciences*, 12(18), 5393–5414, doi:10.5194/bg-12-
724 5393-2015, 2015.
- 725 Bergamaschi, P., Corazza, M., Karstens, U., Athanassiadou, M., Thompson, R. L., Pison, I.,
726 Manning, A. J., Bousquet, P., Segers, A., Vermeulen, A. T., Janssens-Maenhout, G., Schmidt,
727 M., Ramonet, M., Meinhardt, F., Aalto, T., Haszpra, L., Moncrieff, J., Popa, M. E., Lowry,
728 D., Steinbacher, M., Jordan, A., O’Doherty, S., Piacentino, S. and Dlugokencky, E.: Top-
729 down estimates of European CH₄ and N₂O emissions based on four different inverse models,
730 *Atmos. Chem. Phys.*, 15(2), 715–736, doi:10.5194/acp-15-715-2015, 2015.
- 731 Bergamaschi, P., Houweling, S., Segers, A., Krol, M., Frankenberg, C., Scheepmaker, R. A.,
732 Dlugokencky, E., Wofsy, S. C., Kort, E. A., Sweeney, C., Schuck, T., Brenninkmeijer, C.,
733 Chen, H., Beck, V. and Gerbig, C.: Atmospheric CH₄ in the first decade of the 21st century:
734 Inverse modeling analysis using SCIAMACHY satellite retrievals and NOAA surface
735 measurements, *J. Geophys. Res. Atmos.*, 118(13), 7350–7369, doi:10.1002/jgrd.50480, 2013.
- 736 Bergamaschi, P., Krol, M., Dentener, F., Vermeulen, A., Meinhardt, F., Graul, R., Ramonet,
737 M., Peters, W. and Dlugokencky, E. J.: Inverse modelling of national and European CH₄
738 emissions using the atmospheric zoom model TM5, *Atmos. Chem. Phys.*, 5(9), 2431–2460,
739 doi:10.5194/acp-5-2431-2005, 2005.
- 740 Bergamaschi, P., Krol, M., Meirink, J. F., Dentener, F., Segers, A., van Aardenne, J., Monni,
741 S., Vermeulen, A. T., Schmidt, M., Ramonet, M., Yver, C., Meinhardt, F., Nisbet, E. G.,
742 Fisher, R. E., O’Doherty, S. and Dlugokencky, E. J.: Inverse modeling of European CH₄
743 emissions 2001–2006, *J. Geophys. Res. Atmos.*, 115(D22), D22309,
744 doi:10.1029/2010JD014180, 2010.
- 745 Bhattacharya, S. K., Borole, D. V., Francey, R. J., Allison, C. E., Steele, L. P., Krummel, P.,
746 Langenfelds, R., Masarie, K. A., Tiwari, Y. K. and Patra, P. K.: Trace gases and CO₂ isotope
747 records from Cabo de Rama, India, *Curr. Sci.*, 97(9), 1336–1344, 2009.
- 748 Biraud, S., Ciais, P., Ramonet, M., Simmonds, P., Kazan, V., Monfray, P., O’Doherty, S.,
749 Spain, T. G. and Jennings, S. G.: European greenhouse gas emissions estimated from
750 continuous atmospheric measurements and ²²²Rn at Mace Head, Ireland, *J. Geophys. Res.*
751 *Atmos.*, 105(D1), 1351–1366, doi:10.1029/1999JD900821, 2000.

752 Boden, T. A., Marland, G. and Andres, R. J.: Global, Regional, and National Fossil-Fuel CO₂
753 Emissions, Oak Ridge, Tenn., USA., 2015.

754 Bousquet, P., Ciais, P., Miller, J. B., Dlugokencky, E. J., Hauglustaine, D. A., Prigent, C.,
755 Van der Werf, G. R., Peylin, P., Brunke, E.-G., Carouge, C., Langenfelds, R. L., Lathiere, J.,
756 Papa, F., Ramonet, M., Schmidt, M., Steele, L. P., Tyler, S. C. and White, J.: Contribution of
757 anthropogenic and natural sources to atmospheric methane variability, *Nature*, 443(7110),
758 439–443 [online] Available from: <http://dx.doi.org/10.1038/nature05132>, 2006.

759 Bousquet, P., Peylin, P., Ciais, P., Le Quéré, C., Friedlingstein, P. and Tans, P. P.: Regional
760 changes in carbon dioxide fluxes of land and oceans since 1980, *Science* (80-.), 290(5495),
761 1342–1346 [online] Available from:
762 <http://science.sciencemag.org/content/290/5495/1342.abstract>, 2000.

763 Bruhwiler, L., Dlugokencky, E., Masarie, K., Ishizawa, M., Andrews, A., Miller, J., Sweeney,
764 C., Tans, P. and Worthy, D.: CarbonTracker-CH₄: an assimilation system for estimating
765 emissions of atmospheric methane, *Atmos. Chem. Phys.*, 14(16), 8269–8293,
766 doi:10.5194/acp-14-8269-2014, 2014.

767 Cadule, P., Friedlingstein, P., Bopp, L., Sitch, S., Jones, C. D., Ciais, P., Piao, S. L. and
768 Peylin, P.: Benchmarking coupled climate-carbon models against long-term atmospheric CO₂
769 measurements, *Global Biogeochem. Cycles*, 24(2), GB2016, doi:10.1029/2009GB003556,
770 2010.

771 Chen, Y.-H. and Prinn, R. G.: Atmospheric modeling of high- and low-frequency methane
772 observations: Importance of interannually varying transport, *J. Geophys. Res. Atmos.*,
773 110(D10), D10303, doi:10.1029/2004JD005542, 2005.

774 Chevillard, A., Karstens, U. T. E., Ciais, P., Lafont, S. and Heimann, M.: Simulation of
775 atmospheric CO₂ over Europe and western Siberia using the regional scale model REMO,
776 *Tellus B*, 54(5), 872–894, doi:10.1034/j.1600-0889.2002.01340.x, 2002.

777 Denning, A. S., Fung, I. Y. and Randall, D.: Latitudinal gradient of atmospheric CO₂ due to
778 seasonal exchange with land biota, *Nature*, 376(6537), 240–243, doi:10.1038/376240a0, 1995.

779 Denning, A. S., Randall, D. A., Collatz, G. J. and Sellers, P. J.: Simulations of terrestrial
780 carbon metabolism and atmospheric CO₂ in a general circulation model, *Tellus B*, 48(4),
781 543–567, doi:10.1034/j.1600-0889.1996.t01-1-00010.x, 1996.

782 Dlugokencky, E. J., Steele, L. P., Lang, P. M. and Masarie, K. A.: Atmospheric methane at
783 Mauna Loa and Barrow observatories: Presentation and analysis of in situ measurements, *J.*
784 *Geophys. Res. Atmos.*, 100(D11), 23103–23113, doi:10.1029/95JD02460, 1995.

785 Fang, S., Tans, P. P., Dong, F., Zhou, H. and Luan, T.: Characteristics of atmospheric CO₂
786 and CH₄ at the Shangdianzi regional background station in China, *Atmos. Environ.*, 131, 1–8,
787 doi:<http://dx.doi.org/10.1016/j.atmosenv.2016.01.044>, 2016.

788 Fang, S. X., Zhou, L. X., Tans, P. P., Ciais, P., Steinbacher, M., Xu, L. and Luan, T.: In situ
789 measurement of atmospheric CO₂ at the four WMO/GAW stations in China, *Atmos. Chem.*
790 *Phys.*, 14(5), 2541–2554, doi:10.5194/acp-14-2541-2014, 2014.

791 Feng, L., Palmer, P. I., Yang, Y., Yantosca, R. M., Kawa, S. R., Paris, J.-D., Matsueda, H.
792 and Machida, T.: Evaluating a 3-D transport model of atmospheric CO₂ using ground-based,
793 aircraft, and space-borne data, *Atmos. Chem. Phys.*, 11(6), 2789–2803, doi:10.5194/acp-11-
794 2789-2011, 2011.

795 Folberth, G. A., Hauglustaine, D. A., Lathière, J. and Brocheton, F.: Interactive chemistry in
796 the Laboratoire de Météorologie Dynamique general circulation model: model description
797 and impact analysis of biogenic hydrocarbons on tropospheric chemistry, *Atmos. Chem.*
798 *Phys.*, 6(8), 2273–2319, doi:10.5194/acp-6-2273-2006, 2006.

799 Ganesan, A. L., Chatterjee, A., Prinn, R. G., Harth, C. M., Salameh, P. K., Manning, A. J.,
800 Hall, B. D., Mühle, J., Meredith, L. K., Weiss, R. F., O’Doherty, S. and Young, D.: The
801 variability of methane, nitrous oxide and sulfur hexafluoride in Northeast India, *Atmos.*
802 *Chem. Phys.*, 13(21), 10633–10644, doi:10.5194/acp-13-10633-2013, 2013.

803 Geels, C., Doney, S. C., Dargaville, R., Brandt, J. and Christensen, J. H.: Investigating the
804 sources of synoptic variability in atmospheric CO₂ measurements over the Northern
805 Hemisphere continents: a regional model study, *Tellus B*, 56(1), 35–50, doi:10.1111/j.1600-
806 0889.2004.00084.x, 2004.

807 Geels, C., Gloor, M., Ciais, P., Bousquet, P., Peylin, P., Vermeulen, A. T., Dargaville, R.,
808 Aalto, T., Brandt, J., Christensen, J. H., Frohn, L. M., Haszpra, L., Karstens, U., Rödenbeck,
809 C., Ramonet, M., Carboni, G. and Santaguida, R.: Comparing atmospheric transport models
810 for future regional inversions over Europe – Part 1: mapping the atmospheric CO₂
811 signals, *Atmos. Chem. Phys.*, 7(13), 3461–3479, doi:10.5194/acp-7-3461-2007, 2007a.

812 Geels, C., Gloor, M., Ciais, P., Bousquet, P., Peylin, P., Vermeulen, A. T., Dargaville, R.,
813 Aalto, T., Brandt, J., Christensen, J. H., Frohn, L. M., Haszpra, L., Karstens, U., Rödenbeck,
814 C., Ramonet, M., Carboni, G. and Santaguida, R.: Comparing atmospheric transport models
815 for future regional inversions over Europe – Part 1: mapping the atmospheric CO₂
816 signals, *Atmos. Chem. Phys.*, 7(13), 3461–3479, doi:10.5194/acp-7-3461-2007, 2007b.

817 Griffiths, A. D., Conen, F., Weingartner, E., Zimmermann, L., Chambers, S. D., Williams, A.
818 G. and Steinbacher, M.: Surface-to-mountaintop transport characterised by radon
819 observations at the Jungfraujoch, *Atmos. Chem. Phys.*, 14(23), 12763–12779,
820 doi:10.5194/acp-14-12763-2014, 2014.

821 Gurney, K. R., Law, R. M., Denning, A. S., Rayner, P. J., Baker, D., Bousquet, P., Bruhwiler,
822 L., Chen, Y.-H., Ciais, P., Fan, S., Fung, I. Y., Gloor, M., Heimann, M., Higuchi, K., John, J.,
823 Maki, T., Maksyutov, S., Masarie, K., Peylin, P., Prather, M., Pak, B. C., Randerson, J.,
824 Sarmiento, J., Taguchi, S., Takahashi, T. and Yuen, C.-W.: Towards robust regional
825 estimates of CO₂ sources and sinks using atmospheric transport models, *Nature*, 415(6872),
826 626–630 [online] Available from: <http://dx.doi.org/10.1038/415626a>, 2002.

827 Haszpra, L.: Carbon dioxide concentration measurements at a rural site in Hungary, *Tellus B*,
828 47(1–2), 17–22, doi:10.1034/j.1600-0889.47.issue1.3.x, 1995.

829 Hauglustaine, D. A., Balkanski, Y. and Schulz, M.: A global model simulation of present and
830 future nitrate aerosols and their direct radiative forcing of climate, *Atmos. Chem. Phys.*,
831 14(20), 11031–11063, doi:10.5194/acp-14-11031-2014, 2014.

832 Hauglustaine, D. A., Hourdin, F., Jourdain, L., Filiberti, M.-A., Walters, S., Lamarque, J.-F.
833 and Holland, E. A.: Interactive chemistry in the Laboratoire de Météorologie Dynamique
834 general circulation model: Description and background tropospheric chemistry evaluation, *J.*
835 *Geophys. Res. Atmos.*, 109(D4), D04314, doi:10.1029/2003JD003957, 2004.

836 Hourdin, F., Couvreux, F., Menut, L., Hourdin, F., Couvreux, F. and Menut, L.:
837 Parameterization of the Dry Convective Boundary Layer Based on a Mass Flux
838 Representation of Thermals, *J. Atmos. Sci.*, 59(6), 1105–1123, doi:10.1175/1520-

839 0469(2002)059<1105:POTDCB>2.0.CO;2, 2002.

840 Hourdin, F. and Issartel, J.-P.: Sub-surface nuclear tests monitoring through the CTBT Xenon
841 Network, *Geophys. Res. Lett.*, 27(15), 2245–2248, doi:10.1029/1999GL010909, 2000.

842 Hourdin, F., Musat, I., Bony, S., Braconnot, P., Codron, F., Dufresne, J.-L., Fairhead, L.,
843 Filiberti, M.-A., Friedlingstein, P., Grandpeix, J.-Y., Krinner, G., LeVan, P., Li, Z.-X. and
844 Lott, F.: The LMDZ4 general circulation model: climate performance and sensitivity to
845 parametrized physics with emphasis on tropical convection, *Clim. Dyn.*, 27(7–8), 787–813,
846 doi:10.1007/s00382-006-0158-0, 2006.

847 Houweling, S., Badawy, B., Baker, D. F., Basu, S., Belikov, D., Bergamaschi, P., Bousquet,
848 P., Broquet, G., Butler, T., Canadell, J. G., Chen, J., Chevallier, F., Ciais, P., Collatz, G. J.,
849 Denning, S., Engelen, R., Enting, I. G., Fischer, M. L., Fraser, A., Gerbig, C., Gloor, M.,
850 Jacobson, A. R., Jones, D. B. A., Heimann, M., Khalil, A., Kaminski, T., Kasibhatla, P. S.,
851 Krakauer, N. Y., Krol, M., Maki, T., Maksyutov, S., Manning, A., Meesters, A., Miller, J. B.,
852 Palmer, P. I., Patra, P., Peters, W., Peylin, P., Poussi, Z., Prather, M. J., Randerson, J. T.,
853 Röckmann, T., Rödenbeck, C., Sarmiento, J. L., Schimel, D. S., Scholze, M., Schuh, A.,
854 Suntharalingam, P., Takahashi, T., Turnbull, J., Yurganov, L. and Vermeulen, A.: Iconic
855 CO₂ Time Series at Risk, *Science* (80-.), 337(6098), 1038–1040 [online] Available from:
856 <http://science.sciencemag.org/content/337/6098/1038.2.abstract>, 2012.

857 Huntzinger, D. N., Schwalm, C., Michalak, A. M., Schaefer, K., King, A. W., Wei, Y.,
858 Jacobson, A., Liu, S., Cook, R. B., Post, W. M., Berthier, G., Hayes, D., Huang, M., Ito, A.,
859 Lei, H., Lu, C., Mao, J., Peng, C. H., Peng, S., Poulter, B., Riccuto, D., Shi, X., Tian, H.,
860 Wang, W., Zeng, N., Zhao, F. and Zhu, Q.: The North American Carbon Program Multi-
861 Scale Synthesis and Terrestrial Model Intercomparison Project – Part 1: Overview and
862 experimental design, *Geosci. Model Dev.*, 6(6), 2121–2133, doi:10.5194/gmd-6-2121-2013,
863 2013.

864 JMA and WMO: WMO WDCGG Data Summary (WDCGG No. 38) Volume IV -
865 Greenhouse Gases and other Atmospheric Gases. [online] Available from:
866 <http://ds.data.jma.go.jp/gmd/wdcgg/pub/products/summary/sum38/sum38.pdf>, 2014.

867 Kaplan, J. O., Folberth, G. and Hauglustaine, D. A.: Role of methane and biogenic volatile
868 organic compound sources in late glacial and Holocene fluctuations of atmospheric methane
869 concentrations, *Global Biogeochem. Cycles*, 20(2), GB2016, doi:10.1029/2005GB002590,
870 2006.

871 Krol, M., Houweling, S., Bregman, B., van den Broek, M., Segers, A., van Velthoven, P.,
872 Peters, W., Dentener, F. and Bergamaschi, P.: The two-way nested global chemistry-transport
873 zoom model TM5: algorithm and applications, *Atmos. Chem. Phys.*, 5(2), 417–432,
874 doi:10.5194/acp-5-417-2005, 2005.

875 Lambert, G. and Schmidt, S.: Reevaluation of the oceanic flux of methane: Uncertainties and
876 long term variations, *Chemosphere*, 26(1–4), 579–589, doi:http://dx.doi.org/10.1016/0045-
877 6535(93)90443-9, 1993.

878 Law, R. M., Peters, W., Rödenbeck, C., Aulagnier, C., Baker, I., Bergmann, D. J., Bousquet,
879 P., Brandt, J., Bruhwiler, L., Cameron-Smith, P. J., Christensen, J. H., Delage, F., Denning, A.
880 S., Fan, S., Geels, C., Houweling, S., Imasu, R., Karstens, U., Kawa, S. R., Kleist, J., Krol, M.
881 C., Lin, S.-J., Lokupitiya, R., Maki, T., Maksyutov, S., Niwa, Y., Onishi, R., Parazoo, N.,
882 Patra, P. K., Pieterse, G., Rivier, L., Satoh, M., Serrar, S., Taguchi, S., Takigawa, M.,

883 Vautard, R., Vermeulen, A. T. and Zhu, Z.: TransCom model simulations of hourly
884 atmospheric CO₂: Experimental overview and diurnal cycle results for 2002, *Global*
885 *Biogeochem. Cycles*, 22(3), GB3009, doi:10.1029/2007GB003050, 2008.

886 Law, R. M., Rayner, P. J., Denning, A. S., Erickson, D., Fung, I. Y., Heimann, M., Piper, S.
887 C., Ramonet, M., Taguchi, S., Taylor, J. A., Trudinger, C. M. and Watterson, I. G.:
888 Variations in modeled atmospheric transport of carbon dioxide and the consequences for CO₂
889 inversions, *Global Biogeochem. Cycles*, 10(4), 783–796, doi:10.1029/96GB01892, 1996.

890 Levin, I., Ciais, P., Langenfelds, R., Schmidt, M., Ramonet, M., Sidorov, K., Tchebakova, N.,
891 Gloor, M., Heimann, M., Schulze, E.-D., Vygodskaya, N. N., Shibistova, O. and Lloyd, J.:
892 Three years of trace gas observations over the EuroSiberian domain derived from aircraft
893 sampling — a concerted action, *Tellus B*, 54(5), 696–712, doi:10.1034/j.1600-
894 0889.2002.01352.x, 2002.

895 Levin, I., Graul, R. and Trivett, N. B. A.: Long-term observations of atmospheric CO₂ and
896 carbon isotopes at continental sites in Germany, *Tellus B*, 47(1–2), 23–34,
897 doi:10.1034/j.1600-0889.47.issue1.4.x, 1995.

898 Lin, X., Indira, N. K., Ramonet, M., Delmotte, M., Ciais, P., Bhatt, B. C., Reddy, M. V.,
899 Angchuk, D., Balakrishnan, S., Jorphail, S., Dorjai, T., Mahey, T. T., Patnaik, S., Begum, M.,
900 Brenninkmeijer, C., Durairaj, S., Kirubakaran, R., Schmidt, M., Swathi, P. S., Vinithkumar,
901 N. V., Yver Kwok, C. and Gaur, V. K.: Long-lived atmospheric trace gases measurements in
902 flask samples from three stations in India, *Atmos. Chem. Phys.*, 15(17), 9819–9849,
903 doi:10.5194/acp-15-9819-2015, 2015.

904 Locatelli, R.: Estimation des sources et puits de méthane: bilan planétaire et impacts de la
905 modélisation du transport atmosphérique, Versailles-St Quentin en Yvelines, France. [online]
906 Available from: <http://www.theses.fr/2014VERS0035>, 2014.

907 Locatelli, R., Bousquet, P., Chevallier, F., Fortems-Cheney, A., Szopa, S., Saunois, M.,
908 Agusti-Panareda, A., Bergmann, D., Bian, H., Cameron-Smith, P., Chipperfield, M. P., Gloor,
909 E., Houweling, S., Kawa, S. R., Krol, M., Patra, P. K., Prinn, R. G., Rigby, M., Saito, R. and
910 Wilson, C.: Impact of transport model errors on the global and regional methane emissions
911 estimated by inverse modelling, *Atmos. Chem. Phys.*, 13(19), 9917–9937, doi:10.5194/acp-
912 13-9917-2013, 2013.

913 Locatelli, R., Bousquet, P., Hourdin, F., Saunois, M., Cozic, A., Couvreux, F., Grandpeix, J.-
914 Y., Lefebvre, M.-P., Rio, C., Bergamaschi, P., Chambers, S. D., Karstens, U., Kazan, V., van
915 der Laan, S., Meijer, H. A. J., Moncrieff, J., Ramonet, M., Scheeren, H. A., Schlosser, C.,
916 Schmidt, M., Vermeulen, A. and Williams, A. G.: Atmospheric transport and chemistry of
917 trace gases in LMDz5B: evaluation and implications for inverse modelling, *Geosci. Model*
918 *Dev.*, 8(2), 129–150, doi:10.5194/gmd-8-129-2015, 2015a.

919 Locatelli, R., Bousquet, P., Hourdin, F., Saunois, M., Cozic, A., Couvreux, F., Grandpeix, J.-
920 Y., Lefebvre, M.-P., Rio, C., Bergamaschi, P., Chambers, S. D., Karstens, U., Kazan, V., Van
921 Der Laan, S., Meijer, H. A. J., Moncrieff, J., Ramonet, M., Scheeren, H. A., Schlosser, C.,
922 Schmidt, M., Vermeulen, A. and Williams, A. G.: Atmospheric transport and chemistry of
923 trace gases in LMDz5B: evaluation and implications for inverse modelling, *Geosci. Model*
924 *Dev.*, 8, 129–150, doi:10.5194/gmd-8-129-2015, 2015b.

925 Locatelli, R., Bousquet, P., Saunois, M., Chevallier, F. and Cressot, C.: Sensitivity of the
926 recent methane budget to LMDz sub-grid-scale physical parameterizations, *Atmos. Chem.*

- 927 Phys, 15, 9765–9780, doi:10.5194/acp-15-9765-2015, 2015c.
- 928 Lopez, M., Schmidt, M., Ramonet, M., Bonne, J.-L., Colomb, A., Kazan, V., Laj, P. and
929 Pichon, J.-M.: Three years of semicontinuous greenhouse gas measurements at the Puy de
930 Dôme station (central France), *Atmos. Meas. Tech.*, 8(9), 3941–3958, doi:10.5194/amt-8-
931 3941-2015, 2015.
- 932 Louis, J.-F.: A parametric model of vertical eddy fluxes in the atmosphere, *Boundary-Layer*
933 *Meteorol.*, 17(2), 187–202, doi:10.1007/BF00117978, 1979.
- 934 Machida, T., Katsumata, K., Tohjima, Y., Watai, T. and Mukai, H.: Preparing and
935 maintaining of CO₂ calibration scale in National Institute for Environmental Studies: NIES
936 95 CO₂ scale, in Report of the 14th WMO/IAEA Meeting of Experts on Carbon Dioxide
937 Concentration and Related Tracer Measurement Techniques, edited by T. Laurila, pp. 26–29,
938 GMO/GAW Report No. 186, Helsinki., 2009.
- 939 Machida, T., Matsueda, H., Sawa, Y., Nakagawa, Y., Hirotsu, K., Kondo, N., Goto, K.,
940 Nakazawa, T., Ishikawa, K. and Ogawa, T.: Worldwide measurements of atmospheric CO₂
941 and other trace gas species using commercial airlines, *J. Atmos. Ocean. Technol.*, 25(10),
942 1744–1754, doi:10.1175/2008JTECHA1082.1, 2008.
- 943 Maksyutov, S., Patra, P. K., Onishi, R., Saeki, T. and Nakazawa, T.: NIES/FRCGC Global
944 Atmospheric Tracer Transport Model: Description, validation, and surface sources and sinks
945 inversion, *J. Earth Simulator*, 9, 3–18, 2008.
- 946 Matthews, E., Fung, I. and Lerner, J.: Methane emission from rice cultivation: Geographic
947 and seasonal distribution of cultivated areas and emissions, *Global Biogeochem. Cycles*, 5(1),
948 3–24, doi:10.1029/90GB02311, 1991.
- 949 Miles, N. L., Richardson, S. J., Davis, K. J., Lauvaux, T., Andrews, A. E., West, T. O.,
950 Bandaru, V. and Crosson, E. R.: Large amplitude spatial and temporal gradients in
951 atmospheric boundary layer CO₂ mole fractions detected with a tower-based network in the
952 U.S. upper Midwest, *J. Geophys. Res. Biogeosciences*, 117(G1), n/a-n/a,
953 doi:10.1029/2011JG001781, 2012.
- 954 Olivier, J. G. J., Janssens-Maenhout, G., Muntean, M. and Peters, J. A. H. W.: Trends in
955 global CO₂ emissions: 2015 Report., 2015.
- 956 Parazoo, N. C., Denning, A. S., Kawa, S. R., Corbin, K. D., Lokupitiya, R. S. and Baker, I. T.:
957 Mechanisms for synoptic variations of atmospheric CO₂ in North America, South America
958 and Europe, *Atmos. Chem. Phys.*, 8(23), 7239–7254, doi:10.5194/acp-8-7239-2008, 2008.
- 959 Park, G., Wanninkhof, R. I. F., Doney, S. C., Takahashi, T., Lee, K., Feely, R. A., Sabine, C.
960 L., Triñanes, J. and Lima, I. D.: Variability of global net sea–air CO₂ fluxes over the last
961 three decades using empirical relationships, *Tellus B*, 62(5), 352–368, doi:10.1111/j.1600-
962 0889.2010.00498.x, 2010.
- 963 Patra, P. K., Canadell, J. G., Houghton, R. A., Piao, S. L., Oh, N.-H., Ciais, P., Manjunath, K.
964 R., Chhabra, A., Wang, T., Bhattacharya, T., Bousquet, P., Hartman, J., Ito, A., Mayorga, E.,
965 Niwa, Y., Raymond, P. A., Sarma, V. V. S. S. and Lasco, R.: The carbon budget of South
966 Asia, *Biogeosciences*, 10(1), 513–527, doi:10.5194/bg-10-513-2013, 2013.
- 967 Patra, P. K., Houweling, S., Krol, M., Bousquet, P., Belikov, D., Bergmann, D., Bian, H.,
968 Cameron-Smith, P., Chipperfield, M. P., Corbin, K., Fortems-Cheiney, A., Fraser, A., Gloor,
969 E., Hess, P., Ito, A., Kawa, S. R., Law, R. M., Loh, Z., Maksyutov, S., Meng, L., Palmer, P. I.,

- 970 Prinn, R. G., Rigby, M., Saito, R. and Wilson, C.: TransCom model simulations of CH₄ and
971 related species: linking transport, surface flux and chemical loss with CH₄ variability in the
972 troposphere and lower stratosphere, *Atmos. Chem. Phys.*, 11(24), 12813–12837,
973 doi:10.5194/acp-11-12813-2011, 2011.
- 974 Patra, P. K., Law, R. M., Peters, W., Rödenbeck, C., Takigawa, M., Aulagnier, C., Baker, I.,
975 Bergmann, D. J., Bousquet, P., Brandt, J., Bruhwiler, L., Cameron-Smith, P. J., Christensen, J.
976 H., Delage, F., Denning, A. S., Fan, S., Geels, C., Houweling, S., Imasu, R., Karstens, U.,
977 Kawa, S. R., Kleist, J., Krol, M. C., Lin, S.-J., Lokupitiya, R., Maki, T., Maksyutov, S., Niwa,
978 Y., Onishi, R., Parazoo, N., Pieterse, G., Rivier, L., Satoh, M., Serrar, S., Taguchi, S.,
979 Vautard, R., Vermeulen, A. T. and Zhu, Z.: TransCom model simulations of hourly
980 atmospheric CO₂: Analysis of synoptic-scale variations for the period 2002–2003, *Global*
981 *Biogeochem. Cycles*, 22(4), GB4013, doi:10.1029/2007GB003081, 2008.
- 982 Patra, P. K., Takigawa, M., Dutton, G. S., Uhse, K., Ishijima, K., Lintner, B. R., Miyazaki, K.
983 and Elkins, J. W.: Transport mechanisms for synoptic, seasonal and interannual SF₆
984 variations and “age” of air in troposphere, *Atmos. Chem. Phys.*, 9(4), 1209–1225,
985 doi:10.5194/acp-9-1209-2009, 2009a.
- 986 Patra, P., Takigawa, M., Ishijima, K., Choi, B.-C., Cunnold, D., J. Dlugokencky, E., Fraser,
987 P., J. Gomez-Pelaez, A., Goo, T.-Y., Kim, J.-S., Krummel, P., Langenfelds, R., Meinhardt, F.,
988 Mukai, H., O’Doherty, S., G. Prinn, R., Simmonds, P., Steele, P., Tohjima, Y., Tsuboi, K.,
989 Uhse, K., Weiss, R., Worthy, D. and Nakazawa, T.: Growth rate, seasonal, synoptic, diurnal
990 variations and budget of methane in the lower atmosphere, *J. Meteorol. Soc. Japan. Ser. II*,
991 87(4), 635–663, 2009b.
- 992 Peng, S., Ciais, P., Chevallier, F., Peylin, P., Cadule, P., Sitch, S., Piao, S., Ahlström, A.,
993 Huntingford, C., Levy, P., Li, X., Liu, Y., Lomas, M., Poulter, B., Viovy, N., Wang, T.,
994 Wang, X., Zaehle, S., Zeng, N., Zhao, F. and Zhao, H.: Benchmarking the seasonal cycle of
995 CO₂ fluxes simulated by terrestrial ecosystem models, *Global Biogeochem. Cycles*, 29(1),
996 46–64, doi:10.1002/2014GB004931, 2015.
- 997 Peng, S. S., Piao, S. L., Bousquet, P., Ciais, P., Li, B. G., Lin, X., Tao, S., Wang, Z. P.,
998 Zhang, Y. and Zhou, F.: Inventory of anthropogenic methane emissions in Mainland China
999 from 1980 to 2010, *Atmos. Chem. Phys. Discuss.*, 2016, 1–29, doi:10.5194/acp-2016-139,
1000 2016.
- 1001 Pérez-Landa, G., Ciais, P., Sanz, M. J., Gioli, B., Miglietta, F., Palau, J. L., Gangoiti, G. and
1002 Millán, M. M.: Mesoscale circulations over complex terrain in the Valencia coastal region,
1003 Spain – Part 1: Simulation of diurnal circulation regimes, *Atmos. Chem. Phys.*, 7(7), 1835–
1004 1849, doi:10.5194/acp-7-1835-2007, 2007.
- 1005 Peters, W., Krol, M. C., Dlugokencky, E. J., Dentener, F. J., Bergamaschi, P., Dutton, G.,
1006 Velthoven, P. v., Miller, J. B., Bruhwiler, L. and Tans, P. P.: Toward regional-scale modeling
1007 using the two-way nested global model TM5: Characterization of transport using SF₆, *J.*
1008 *Geophys. Res. Atmos.*, 109(D19), D19314, doi:10.1029/2004JD005020, 2004.
- 1009 Peters, W., Krol, M. C., Van Der Werf, G. R., Houweling, S., Jones, C. D., Hughes, J.,
1010 Schaefer, K., Masarie, K. A., Jacobson, A. R., Miller, J. B., Cho, C. H., Ramonet, M.,
1011 Schmidt, M., Ciattaglia, L., Apadula, F., Heltai, D., Meinhardt, F., Di Sarra, A. G., Piacentino,
1012 S., Sferlazzo, D., Aalto, T., Hatakka, J., Ström, J., Haszpra, L., Meijer, H. A. J., Van der
1013 Laan, S., Neubert, R. E. M., Jordan, A., Rodó, X., Morguá, J.-A., Vermeulen, A. T., Popa, E.,
1014 Rozanski, K., Zimnoch, M., Manning, A. C., Leuenberger, M., Uglietti, C., Dolman, A. J.,

- 1015 Ciais, P., Heimann, M. and Tans, P. P.: Seven years of recent European net terrestrial carbon
1016 dioxide exchange constrained by atmospheric observations, *Glob. Chang. Biol.*, 16(4), 1317–
1017 1337, doi:10.1111/j.1365-2486.2009.02078.x, 2010.
- 1018 Pillai, D., Gerbig, C., Ahmadov, R., Rödenbeck, C., Kretschmer, R., Koch, T., Thompson, R.,
1019 Neininger, B. and Lavrié, J. V: High-resolution simulations of atmospheric CO₂ over
1020 complex terrain – representing the Ochsenkopf mountain tall tower, *Atmos. Chem. Phys.*,
1021 11(15), 7445–7464, doi:10.5194/acp-11-7445-2011, 2011.
- 1022 Popa, M. E., Gloor, M., Manning, A. C., Jordan, A., Schultz, U., Haensel, F., Seifert, T. and
1023 Heimann, M.: Measurements of greenhouse gases and related tracers at Bialystok tall tower
1024 station in Poland, *Atmos. Meas. Tech.*, 3(2), 407–427, doi:10.5194/amt-3-407-2010, 2010.
- 1025 Pregger, T., Scholz, Y. and Friedrich, R.: Documentation of the anthropogenic GHG
1026 emission data for Europe provided in the Frame of CarboEurope GHG and CarboEurope IP,
1027 Stuttgart, Germany., 2007.
- 1028 Le Quéré, C., Moriarty, R., Andrew, R. M., Canadell, J. G., Sitch, S., Korsbakken, J. I.,
1029 Friedlingstein, P., Peters, G. P., Andres, R. J., Boden, T. A., Houghton, R. A., House, J. I.,
1030 Keeling, R. F., Tans, P., Arneeth, A., Bakker, D. C. E., Barbero, L., Bopp, L., Chang, J.,
1031 Chevallier, F., Chini, L. P., Ciais, P., Fader, M., Feely, R. A., Gkritzalis, T., Harris, I., Hauck,
1032 J., Ilyina, T., Jain, A. K., Kato, E., Kitidis, V., Klein Goldewijk, K., Koven, C., Landschützer,
1033 P., Lauvset, S. K., Lefèvre, N., Lenton, A., Lima, I. D., Metzl, N., Millero, F., Munro, D. R.,
1034 Murata, A., Nabel, J. E. M. S., Nakaoka, S., Nojiri, Y., O’Brien, K., Olsen, A., Ono, T., Pérez,
1035 F. F., Pfeil, B., Pierrot, D., Poulter, B., Rehder, G., Rödenbeck, C., Saito, S., Schuster, U.,
1036 Schwinger, J., Séférian, R., Steinhoff, T., Stocker, B. D., Sutton, A. J., Takahashi, T.,
1037 Tilbrook, B., van der Laan-Luijkx, I. T., van der Werf, G. R., van Heuven, S., Vandemark, D.,
1038 Viovy, N., Wiltshire, A., Zaehle, S. and Zeng, N.: Global Carbon Budget 2015, *Earth Syst.*
1039 *Sci. Data*, 7(2), 349–396, doi:10.5194/essd-7-349-2015, 2015.
- 1040 Ramonet, M., Ciais, P., Nepomniachii, I., Sidorov, K., Neubert, R. E. M., Langendörfer, U.,
1041 Picard, D., Kazan, V., Biraud, S., Gusti, M., Kolle, O., Schulze, E.-D. and Lloyd, J.: Three
1042 years of aircraft-based trace gas measurements over the Fyodorovskoye southern taiga forest,
1043 300 km north-west of Moscow, *Tellus B*, 54(5), 713–734, doi:10.1034/j.1600-
1044 0889.2002.01358.x, 2002.
- 1045 Randerson, J. T., Chen, Y., van der Werf, G. R., Rogers, B. M. and Morton, D. C.: Global
1046 burned area and biomass burning emissions from small fires, *J. Geophys. Res.*
1047 *Biogeosciences*, 117(G4), n/a-n/a, doi:10.1029/2012JG002128, 2012.
- 1048 Ridgwell, A. J., Marshall, S. J. and Gregson, K.: Consumption of atmospheric methane by
1049 soils: A process-based model, *Global Biogeochem. Cycles*, 13(1), 59–70,
1050 doi:10.1029/1998GB900004, 1999.
- 1051 Rio, C., Hourdin, F., Rio, C. and Hourdin, F.: A Thermal Plume Model for the Convective
1052 Boundary Layer: Representation of Cumulus Clouds, *J. Atmos. Sci.*, 65(2), 407–425,
1053 doi:10.1175/2007JAS2256.1, 2008.
- 1054 Rödenbeck, C., Houweling, S., Gloor, M. and Heimann, M.: CO₂ flux history 1982–2001
1055 inferred from atmospheric data using a global inversion of atmospheric transport, *Atmos.*
1056 *Chem. Phys.*, 3(6), 1919–1964, doi:10.5194/acp-3-1919-2003, 2003.
- 1057 Saeki, T., Saito, R., Belikov, D. and Maksyutov, S.: Global high-resolution simulations of
1058 CO₂ and CH₄ using a NIES transport model to produce a priori concentrations for use in

- 1059 satellite data retrievals, *Geosci. Model Dev.*, 6(1), 81–100, doi:10.5194/gmd-6-81-2013, 2013.
- 1060 Sanderson, M. G.: Biomass of termites and their emissions of methane and carbon dioxide: A
1061 global database, *Global Biogeochem. Cycles*, 10(4), 543–557, doi:10.1029/96GB01893, 1996.
- 1062 Sasakawa, M., Shimoyama, K., Machida, T., Tsuda, N., Suto, H., Arshinov, M., Davydov, D.,
1063 Fofonov, A., Krasnov, O., Saeki, T., Koyama, Y. and Maksyutov, S.: Continuous
1064 measurements of methane from a tower network over Siberia, *Tellus B*, 62(5), 403–416,
1065 doi:10.1111/j.1600-0889.2010.00494.x, 2010.
- 1066 Swathi, P. S., Indira, N. K., Rayner, P. J., Ramonet, M., Jagadheesha, D., Bhatt, B. C. and
1067 Gaur, V. K.: Robust inversion of carbon dioxide fluxes over temperate Eurasia in 2006–2008,
1068 *Curr. Sci.*, 105(2), 201–208, 2013.
- 1069 Szopa, S., Balkanski, Y., Schulz, M., Bekki, S., Cugnet, D., Fortems-Cheiney, A., Turquety,
1070 S., Cozic, A., Déandreis, C., Hauglustaine, D., Idelkadi, A., Lathière, J., Lefevre, F.,
1071 Marchand, M., Vuolo, R., Yan, N. and Dufresne, J.-L.: Aerosol and ozone changes as forcing
1072 for climate evolution between 1850 and 2100, *Clim. Dyn.*, 40(9–10), 2223–2250,
1073 doi:10.1007/s00382-012-1408-y, 2013.
- 1074 Taylor, K. E.: Summarizing multiple aspects of model performance in a single diagram, *J.*
1075 *Geophys. Res. Atmos.*, 106(D7), 7183–7192, doi:10.1029/2000JD900719, 2001.
- 1076 Thompson, R. L., Ishijima, K., Saikawa, E., Corazza, M., Karstens, U., Patra, P. K.,
1077 Bergamaschi, P., Chevallier, F., Dlugokencky, E., Prinn, R. G., Weiss, R. F., O’Doherty, S.,
1078 Fraser, P. J., Steele, L. P., Krummel, P. B., Vermeulen, A., Tohjima, Y., Jordan, A., Haszpra,
1079 L., Steinbacher, M., Van der Laan, S., Aalto, T., Meinhardt, F., Popa, M. E., Moncrieff, J.
1080 and Bousquet, P.: TransCom N₂O model inter-comparison – Part 2: Atmospheric inversion
1081 estimates of N₂O emissions, *Atmos. Chem. Phys.*, 14(12), 6177–6194, doi:10.5194/acp-14-
1082 6177-2014, 2014.
- 1083 Thompson, R. L., Patra, P. K., Chevallier, F., Maksyutov, S., Law, R. M., Ziehn, T., van der
1084 Laan-Luijkx, I. T., Peters, W., Ganshin, A., Zhuravlev, R., Maki, T., Nakamura, T., Shirai, T.,
1085 Ishizawa, M., Saeki, T., Machida, T., Poulter, B., Canadell, J. G. and Ciais, P.: Top-down
1086 assessment of the Asian carbon budget since the mid 1990s, *Nat Commun*, 7 [online]
1087 Available from: <http://dx.doi.org/10.1038/ncomms10724>, 2016.
- 1088 Thompson, R. L., Stohl, A., Zhou, L. X., Dlugokencky, E., Fukuyama, Y., Tohjima, Y., Kim,
1089 S.-Y., Lee, H., Nisbet, E. G., Fisher, R. E., Lowry, D., Weiss, R. F., Prinn, R. G., O’Doherty,
1090 S., Young, D. and White, J. W. C.: Methane emissions in East Asia for 2000–2011 estimated
1091 using an atmospheric Bayesian inversion, *J. Geophys. Res. Atmos.*, 120(9), 4352–4369,
1092 doi:10.1002/2014JD022394, 2015.
- 1093 Thoning, K. W., Tans, P. P. and Komhyr, W. D.: Atmospheric carbon dioxide at Mauna Loa
1094 Observatory: 2. Analysis of the NOAA GMCC data, 1974–1985, *J. Geophys. Res. Atmos.*,
1095 94(D6), 8549–8565, doi:10.1029/JD094iD06p08549, 1989.
- 1096 Tian, H., Lu, C., Ciais, P., Michalak, A. M., Canadell, J. G., Saikawa, E., Huntzinger, D. N.,
1097 Gurney, K. R., Sitch, S., Zhang, B., Yang, J., Bousquet, P., Bruhwiler, L., Chen, G.,
1098 Dlugokencky, E., Friedlingstein, P., Melillo, J., Pan, S., Poulter, B., Prinn, R., Saunio, M.,
1099 Schwalm, C. R. and Wofsy, S. C.: The terrestrial biosphere as a net source of greenhouse
1100 gases to the atmosphere, *Nature*, 531(7593), 225–228 [online] Available from:
1101 <http://dx.doi.org/10.1038/nature16946>, 2016.

1102 Tiedtke, M.: A Comprehensive mass flux scheme for cumulus parameterization in large-scale
1103 models, *Mon. Weather Rev.*, 117(8), 1779–1800, doi:10.1175/1520-
1104 0493(1989)117<1779:ACMFSF>2.0.CO, 1989.

1105 Tiwari, Y. K. and Kumar, R. K.: GHG observation programs in India, *Asian GAW Greenh.*
1106 *Gases Newsl.*, No.3, 5–11, 2012.

1107 Tiwari, Y. K., Vellore, R. K., Ravi Kumar, K., van der Schoot, M. and Cho, C.-H.: Influence
1108 of monsoons on atmospheric CO₂ spatial variability and ground-based monitoring over India,
1109 *Sci. Total Environ.*, 490(0), 570–578, doi:http://dx.doi.org/10.1016/j.scitotenv.2014.05.045,
1110 2014.

1111 Wada, A., Matsueda, H., Sawa, Y., Tsuboi, K. and Okubo, S.: Seasonal variation of
1112 enhancement ratios of trace gases observed over 10 years in the western North Pacific, *Atmos.*
1113 *Environ.*, 45(12), 2129–2137, doi:http://dx.doi.org/10.1016/j.atmosenv.2011.01.043, 2011.

1114 Wang, J.-W., Denning, A. S., Lu, L., Baker, I. T., Corbin, K. D. and Davis, K. J.:
1115 Observations and simulations of synoptic, regional, and local variations in atmospheric CO₂,
1116 *J. Geophys. Res. Atmos.*, 112(D4), D04108, doi:10.1029/2006JD007410, 2007.

1117 Wang, R., Balkanski, Y., Boucher, O., Ciais, P., Schuster, G. L., Chevallier, F., Samset, B. H.,
1118 Liu, J., Piao, S., Valari, M. and Tao, S.: Estimation of global black carbon direct radiative
1119 forcing and its uncertainty constrained by observations, *J. Geophys. Res. Atmos.*, 121(10),
1120 5948–5971, doi:10.1002/2015JD024326, 2016.

1121 Wang, R., Tao, S., Balkanski, Y., Ciais, P., Boucher, O., Liu, J., Piao, S., Shen, H., Vuolo, M.
1122 R., Valari, M., Chen, H., Chen, Y., Cozic, A., Huang, Y., Li, B., Li, W., Shen, G., Wang, B.
1123 and Zhang, Y.: Exposure to ambient black carbon derived from a unique inventory and high-
1124 resolution model, *Proc. Natl. Acad. Sci.* [online] Available from:
1125 <http://www.pnas.org/content/early/2014/01/23/1318763111.abstract>, 2014.

1126 Wei, Y., Liu, S., Huntzinger, D. N., Michalak, A. M., Viovy, N., Post, W. M., Schwalm, C.
1127 R., Schaefer, K., Jacobson, A. R., Lu, C., Tian, H., Ricciuto, D. M., Cook, R. B., Mao, J. and
1128 Shi, X.: The North American Carbon Program Multi-scale Synthesis and Terrestrial Model
1129 Intercomparison Project – Part 2: Environmental driver data, *Geosci. Model Dev.*, 7(6),
1130 2875–2893, doi:10.5194/gmd-7-2875-2014, 2014.

1131 Van Der Werf, G. R., Randerson, J. T., Giglio, L., Van Leeuwen, T. T., Chen, Y., Rogers, B.
1132 M., Mu, M., Van Marle, M. J. E., Morton, D. C., Collatz, G. J., Yokelson, R. J. and
1133 Kasibhatla, P. S.: Global fire emissions estimates during 1997–2016, *Earth Syst. Sci. Data*,
1134 95194, 697–720, doi:10.5194/essd-9-697-2017, 2017.

1135 Winderlich, J., Chen, H., Gerbig, C., Seifert, T., Kolle, O., Lavrič, J. V, Kaiser, C., Höfer, A.
1136 and Heimann, M.: Continuous low-maintenance CO₂/CH₄/H₂O measurements at the Zotino
1137 Tall Tower Observatory (ZOTTO) in Central Siberia, *Atmos. Meas. Tech.*, 3(4), 1113–1128,
1138 doi:10.5194/amt-3-1113-2010, 2010.

1139 Yver Kwok, C., Laurent, O., Guemri, A., Philippon, C., Wastine, B., Rella, C. W., Vuillemin,
1140 C., Truong, F., Delmotte, M., Kazan, V., Darding, M., Lebègue, B., Kaiser, C., Xueref-Rémy,
1141 I. and Ramonet, M.: Comprehensive laboratory and field testing of cavity ring-down
1142 spectroscopy analyzers measuring H₂O, CO₂, CH₄ and CO, *Atmos. Meas. Tech.*, 8(9), 3867–
1143 3892, doi:10.5194/amt-8-3867-2015, 2015.

1144

1146 **Tables**

1147 **Table 1** The prescribed CH₄ and CO₂ surface fluxes used as model input. For each trace gas,
 1148 magnitudes of different types of fluxes are given for the year 2010. Total_{global} and Total_{zoom}
 1149 indicate the total flux summarized over the globe and the zoomed region, respectively.

Type of CH ₄ fluxes	Temporal resolution	Spatial resolution	Total _{global} (TgCH ₄ /yr)	Total _{zoom} (TgCH ₄ /yr)	Data source
Anthropogenic – rice	Monthly, interannual	0.1°	38	32	EDGARv4.2FT2010 + Matthews et al (1991)
Anthropogenic – others	Yearly, interannual	0.1°	320	131	EDGARv4.2FT2010
Wetland	Monthly, climatological	1°	175	29	Kaplan et al. (2006)
Biomass burning	Monthly, interannual	0.5°	19	3	GFED v4.1
Termite	Monthly, climatological	1°	19	3	Sanderson et al. (1996)
Soil	Monthly, climatological	1°	-38	-7	Ridgwell et al. (1999)
Ocean	Monthly, climatological	1°	17	3	Lambert & Schmidt (1993)
Total, TgCH ₄ /yr			550	194	
Type of CO ₂ fluxes	Temporal resolution	Spatial resolution	Total _{global} (PgC/yr)	Total _{zoom} (PgC/yr)	Data source
Anthropogenic	Monthly, interannual	1°	8.9	3.6	IER-EDGAR product
Anthropogenic	Daily, interannual	1°			
Anthropogenic	Hourly, interannual	1°			
Biomass burning	Monthly, interannual	0.5°	2.0	0.2	GFED v4.1
Land flux (NEE)	Monthly, interannual	0.5°	-2.7	0.1	OCHIDEE outputs from trunk version r1882
Land flux (NEE)	Daily, interannual	0.5°			
Land flux (NEE)	Hourly, interannual	0.5°			
Ocean flux	Monthly, interannual	4°×5°	-1.3	0.1	NOAA/PMEL & AOML product; Park et al. (2010)
Total, PgC/yr			6.9	3.9	

1150

1151 **Table 2** Stations used in this study. For the column ‘Zoom’, ‘Y’ indicates a station within the zoomed region.

	Code	Station	LON (°)	LAT (°)	ALT (masl)	Contributor	Type	Time periods used in this study	Zoom	CH ₄	CO ₂
1	ALT	Alert, Canada	-62.52	82.45	210	NOAA/ESRL	coastal	Flask: 2006–2013		Y	Y
2	AMS	Amsterdam Island, France	77.54	-37.80	70	LSCE	marine	Flask: 2006–2013		Y	Y
3	AMY	Anmyeon-do, Korea	126.32	36.53	133	KMA	coastal	Continuous: 2006–2013	Y	Y	
4	BKT	Bukit Kototabang, Indonesia	100.32	-0.20	869	BMKG, Empa, NOAA/ESRL	mountain	Flask: 2006–2013 CH ₄ continuous: 2009–2013 CO ₂ continuous: 2010–2013	Y	Y	Y
5	BRW	Barrow, USA	-156.60	71.32	11	NOAA/ESRL	coastal	Continuous: 2006–2013		Y	Y
6	CGO	Cape Grim, Australia	144.68	-40.68	94	NOAA/ESRL	marine	Flask: 2006–2013		Y	Y
7	COI	Cape Ochi-ishi, Japan	145.50	43.16	94	NIES	coastal	Continuous: 2006–2013		Y	
8	CRI	Cape Rama, India	73.83	15.08	66	CSIRO	coastal	Flask: 2009–2013	Y	Y	Y
9	DDR	Mt. Dodaira, Japan	139.18	36.00	840	Saitama	mountain	Continuous: 2006–2013			Y
10	DSI	Dongsha Island, Taiwan, China	116.73	20.70	8	National Central Univ., NOAA/ESRL	marine	Flask: 2010–2013	Y	Y	Y
11	GMI	Mariana Island, Guam	144.66	13.39	5	Univ. of Guam, NOAA/ESRL	marine	Flask: 2006–2013		Y	Y
12	GSN	Gosan, Korea	126.12	33.15	144	NIER	marine	Continous: 2006–2011	Y	Y	Y
13	HAT	Hateruma, Japan	123.81	24.06	47	NIES	marine	Continous: 2006–2013	Y	Y	
14	HLE	Hanle, India	78.96	32.78	4517	LSCE, CSIR4PI, IIA	mountain	Flask: 2006–2013 CH ₄ continuous: 2012–2013 CO ₂ continuous: 2006–2013	Y	Y	Y
15	JFJ	Jungfrauoch, Switzerland	7.99	46.55	3580	Empa	mountain	CH ₄ continuous: 2006–2013 CO ₂ continuous: 2010–2013		Y	Y
16	JIN	Jinsha, China	114.20	29.63	750	CMA	continental	Flask: 2006–2011	Y		Y
17	KIS	Kisai - Saitama	139.55	36.08	13	Saitama	continental	Continous: 2006–2013			Y
18	KZD	Sary Taukum, Kazakhstan	75.57	44.45	412	KSIEMC, NOAA/ESRL	continental	Flask: 2006–2009	Y	Y	Y
19	KZM	Plateau Assy, Kazakhstan	77.87	43.25	2524	KSIEMC, NOAA/ESRL	mountain	Flask: 2006–2009	Y	Y	Y
20	LIN	Lin’an, China	119.72	30.30	139	CMA	continental	Flask: 2006–2011	Y		Y
21	LLN	Lulin, Taiwan, China	120.87	23.47	2867	LAIBS, NOAA/ESRL	mountain	Flask: 2006–2013	Y	Y	Y
22	LON	Longfengshan, China	127.60	44.73	331	CMA	continental	Flask: 2006–2011	Y		Y
23	MHD	Mace Head, Ireland	-9.90	53.33	8	NOAA/ESRL	coastal	Flask: 2006–2013		Y	Y
24	MKW	Mikawa-Ichinomiya, Japan	137.43	34.85	50	Aichi	continental	Continous: 2006–2011	Y		Y

25	MLO	Mauna Loa, USA	-155.58	19.54	3397	NOAA/ESRL	mountain	Continuous: 2006–2013		Y	Y
26	MNM	Minamitori-shima, Japan	153.98	24.28	28	JMA	marine	Continuous: 2006–2013		Y	Y
27	NWR	Niwot Ridge, USA	-105.59	40.05	3523	NOAA/ESRL	mountain	Flask: 2006–2013		Y	Y
28	PBL	Port Blair, India	92.76	11.65	20	LSCE, CSIR4PI, ESSO/NIOT	marine	Flask: 2009–2013	Y	Y	Y
29	PON	Pondicherry, India	79.86	12.01	30	LSCE, CSIR4PI, Pondicherry Univ.	coastal	Flask: 2006–2013 CH ₄ continuous: 2011–2013 CO ₂ continuous: 2011–2013	Y	Y	Y
30	RYO	Ryori, Japan	141.82	39.03	280	JMA	continental	Continuous: 2006–2013		Y	Y
31	SDZ	Shangdianzi, China	117.12	40.65	293	CMA, NOAA/ESRL	continental	Flask: 2009–2013	Y	Y	Y
32	SEY	Mahe Island, Seychelles	55.53	-4.68	7	SBS, NOAA/ESRL	marine	Flask: 2006–2013		Y	Y
33	SNG	Sinhagad, India	73.75	18.35	1600	IITM	mountain	CH ₄ flask: 2010–2013 CO ₂ flask: 2009–2013	Y	Y	Y
34	SPO	South Pole, USA	-24.80	-89.98	2810	NOAA/ESRL	mountain	Flask: 2006–2013		Y	Y
35	TAP	Tae-ahn Peninsula, Korea	126.13	36.73	21	KCAER, NOAA/ESRL	coastal	Flask: 2006–2013	Y	Y	Y
36	UUM	Ulaan Uul, Mongolia	111.10	44.45	1012	MHRI, NOAA/ESRL	continental	Flask: 2006–2013	Y	Y	Y
37	WIS	Negev Desert, Israel	30.86	34.79	482	WIS, AIES, NOAA/ESRL	continental	Flask: 2006–2013		Y	Y
38	WLG	Mt. Waliguan, China	100.90	36.28	3890	CMA, NOAA/ESRL	mountain	Flask: 2006–2013	Y	Y	Y
39	YON	Yonagunijima, Japan	123.02	24.47	50	JMA	marine	Continuous: 2006–2013	Y	Y	Y

1152

1153 Abbreviations:

1154 Aichi – Aichi Air Environment Division, Japan

1155 AIES – Arava Institute for Environmental Studies, Israel

1156 BMKG – Agency for Meteorology, Climatology and Geophysics, Indonesia

1157 CMA – China Meteorological Administration, China

1158 CSIR4PI – Council of Scientific and Industrial Research Fourth Paradigm Institute, India

1159 CSIRO – Commonwealth Scientific and Industrial Research Organisation, Australia

1160 Empa – Swiss Federal Laboratories for Materials Testing and Research, Switzerland

1161 ESSO/NIOT – Earth System Sciences Organisation/National Institute of Ocean Technology, India

1162 IIA – Indian Institute of Astrophysics, India

1163 IITM – Indian Institute of Tropical Meteorology, India

1164 JMA – Japan Meteorological Agency, Japan

1165 KCAER – Korea Centre for Atmospheric Environment Research, Republic of Korea

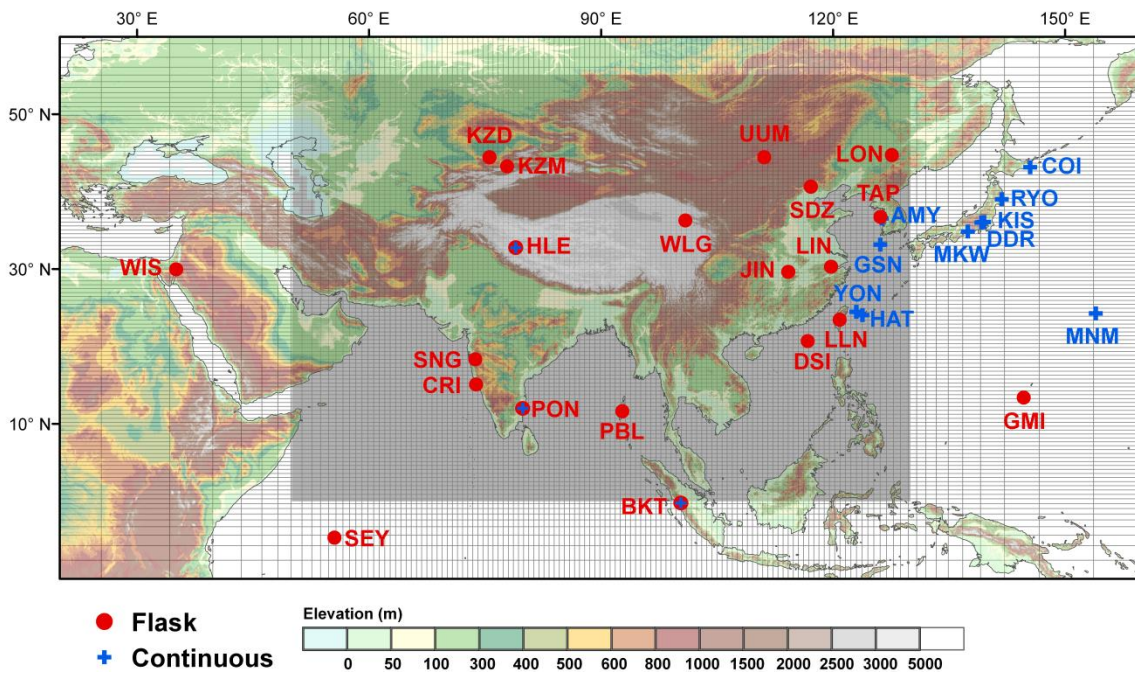
1166 KMA – Korea Meteorological Administration, Republic of Korea

1167 KSIEMC – Kazakh Scientific Institute of Environmental Monitoring and Climate, Kazakhstan

- 1168 LAIBS – Lulin Atmospheric Background Station, Taiwan
- 1169 LSCE – Laboratoire des Sciences du Climat et de l'Environnement, France
- 1170 MHRI – Mongolian Hydrometeorological Research Institute, Mongolia
- 1171 NIER – National Institute of Environmental Research, South Korea
- 1172 NIES – National Institute for Environmental Studies, Japan
- 1173 NIWA – National Institute of Water and Atmospheric Research, New Zealand
- 1174 NOAA/ESRL – National Oceanic and Atmospheric Administration/Earth System Research Laboratory
- 1175 Saitama – Center for Environmental Science in Saitama
- 1176 SBS – Seychelles Bureau of Standards, Seychelles
- 1177 WIS – Weizmann Institute of Science, Israel

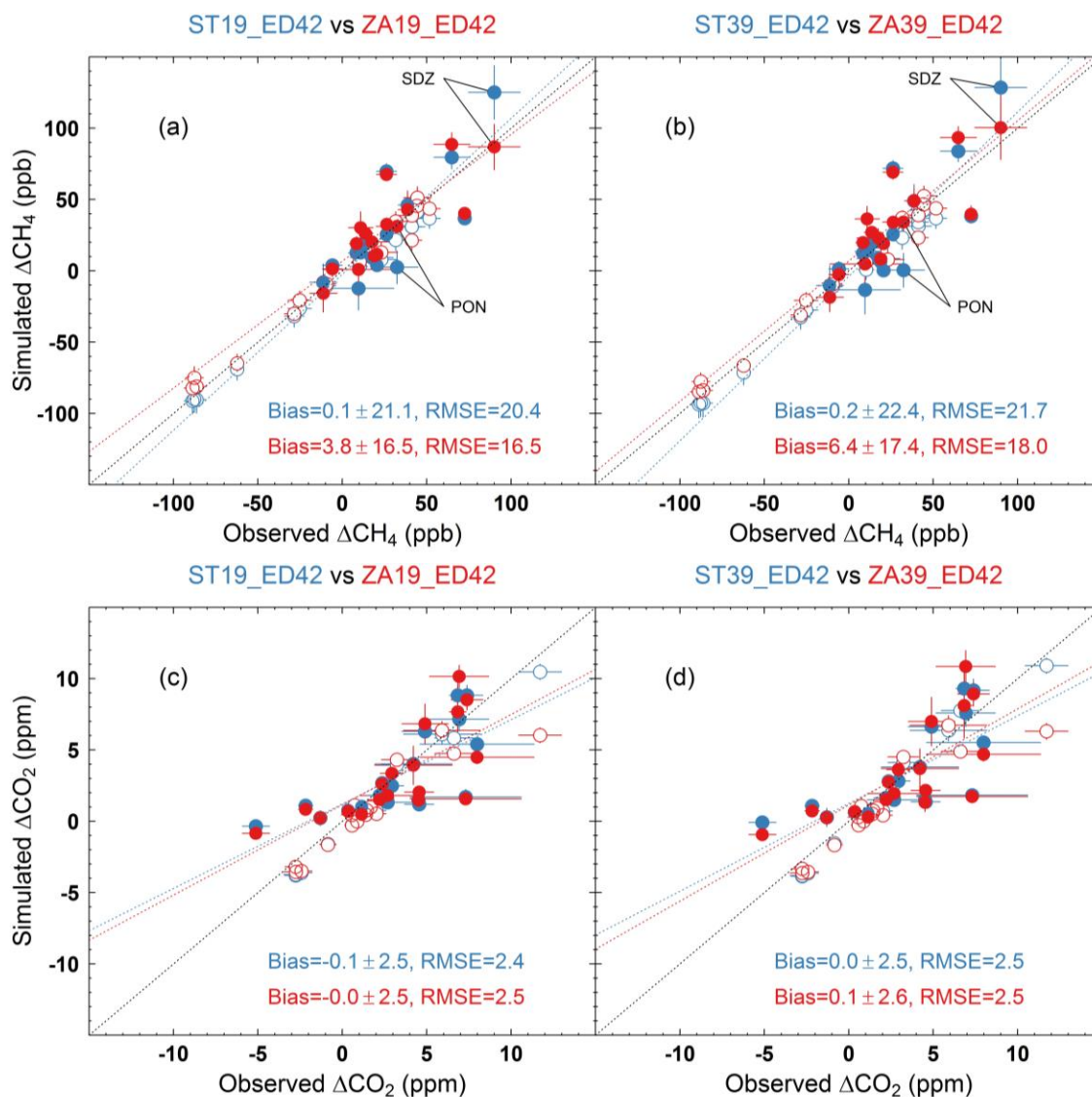
1178 **Figures**

1179 **Figure 1** Map of locations of stations within and around the zoomed region. The zoomed grid
1180 of the LMDz-INCA model is plotted with the NASA Shuttle Radar Topographic Mission
1181 (SRTM) 1km digital elevation data (DEM) as background (<http://srtm.csi.cgiar.org>). The grey
1182 shaded area indicates the region with a horizontal resolution of $\sim 0.66^\circ \times \sim 0.51^\circ$. The red
1183 close circle (blue cross) represents the atmospheric station where flask (continuous)
1184 measurements are available and used in this study.



1185
1186

1187 **Figure 2** Scatterplots of the simulated and observed mean annual gradients of CH₄ (a, b) and
 1188 CO₂ (c, d) between HLE and other stations. In each panel, the simulated CH₄ or CO₂
 1189 gradients are based on model outputs from STs (blue circles) and ZAs (red circles),
 1190 respectively. The black dotted line indicates the identity line, whereas the blue and red dotted
 1191 lines indicates the corresponding linear fitted lines. The closed and open circles represent
 1192 stations inside and outside the zoomed region.



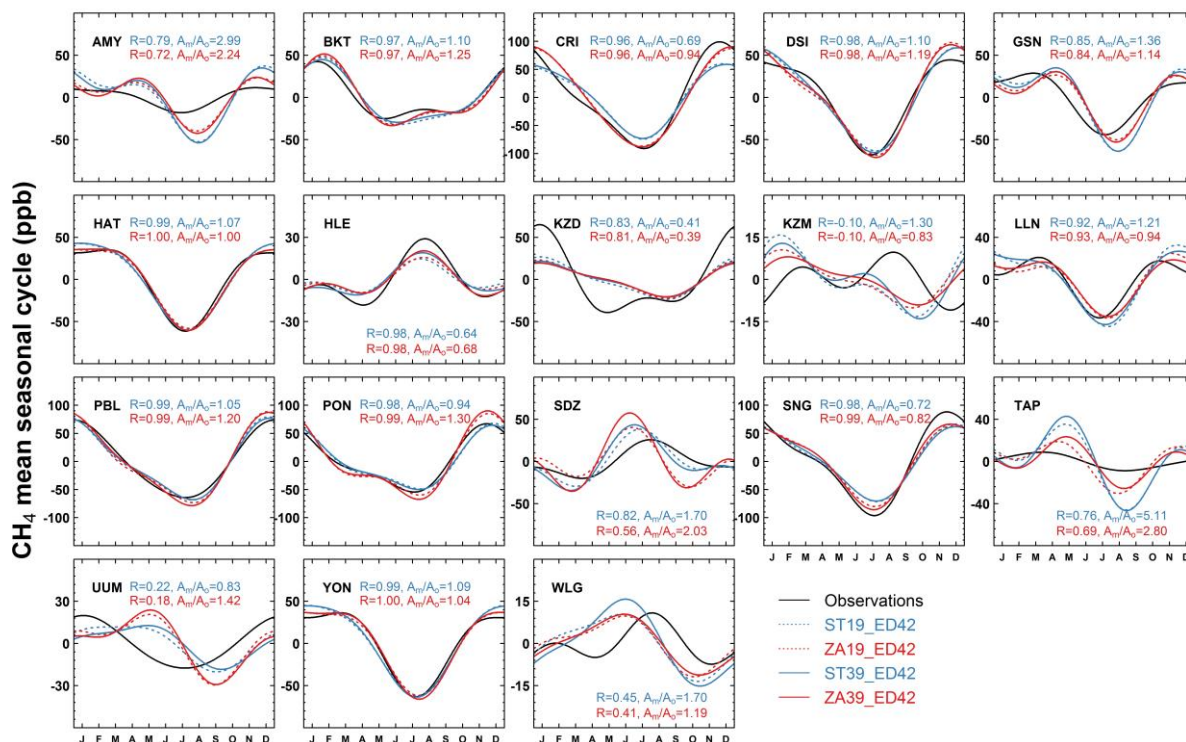
1193

1194

1195

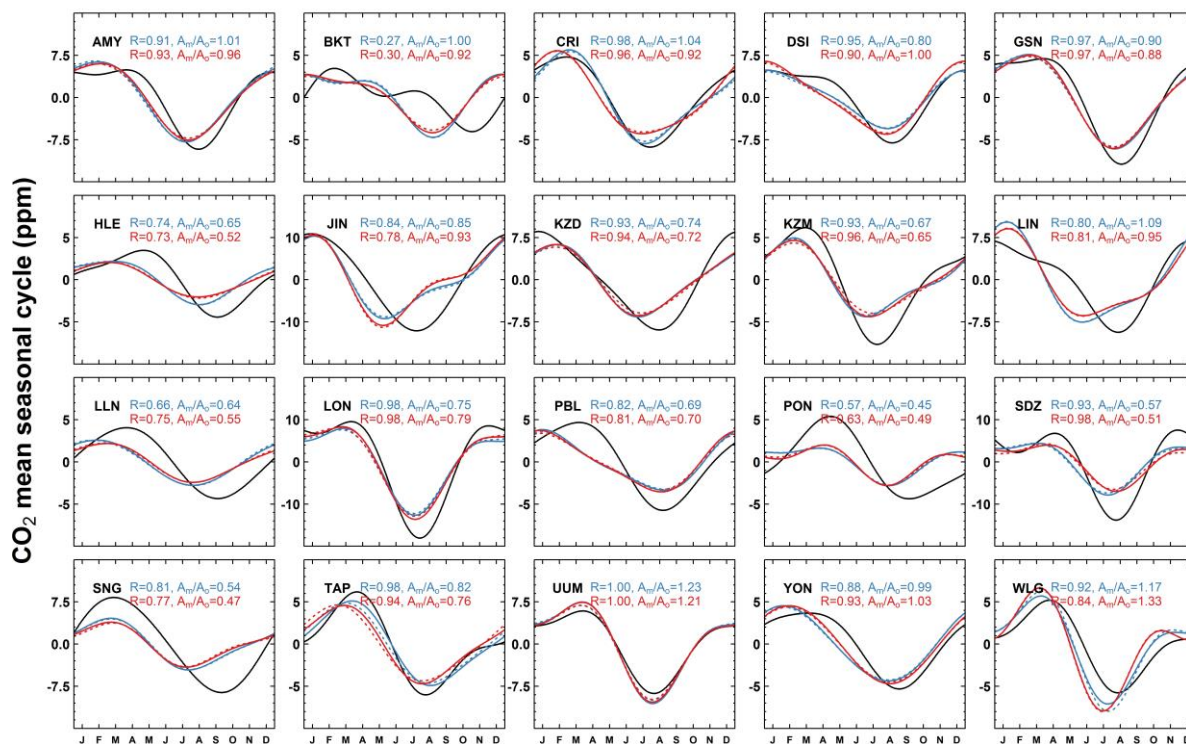
1196 **Figure 3** The observed and simulated mean seasonal cycles of CH₄ (a) and CO₂ (b) for
 1197 stations within the zoomed region. In each panel, the simulated mean seasonal cycles are
 1198 based on model outputs from STs (blue lines) and ZAs (red lines), respectively. The text
 1199 shows statistics between the simulated and observed seasonal cycles for 39-layer models.

1200 (a)



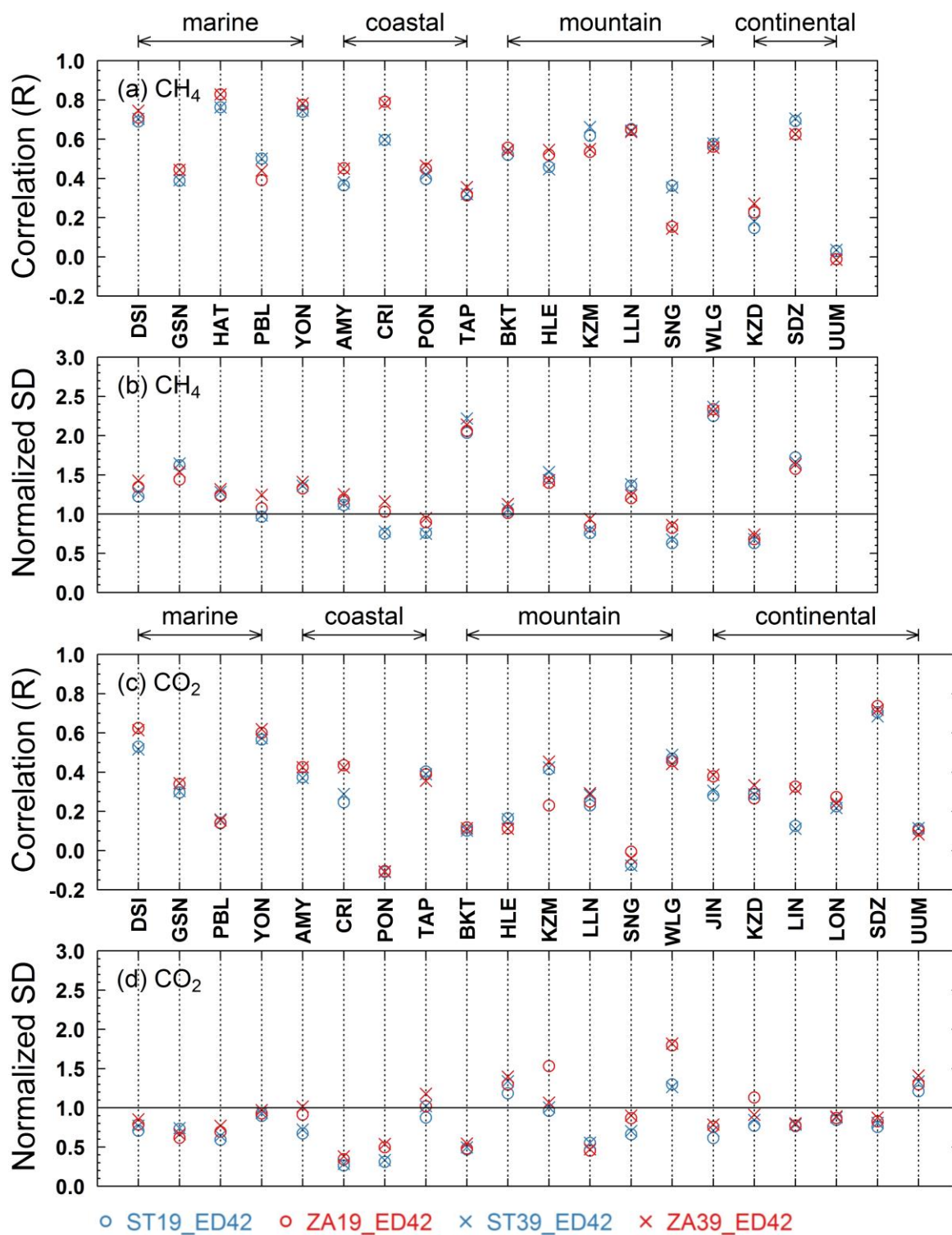
1201
1202

(b)



1203

1204 **Figure 4** The correlations and normalized standard deviations between the simulated and
 1205 observed synoptic variability for CH₄ (a,b) and CO₂ (c,d) at stations within the zoomed
 1206 region. For each station, the synoptic variability is calculated from residuals from the
 1207 smoothed fitting curve.



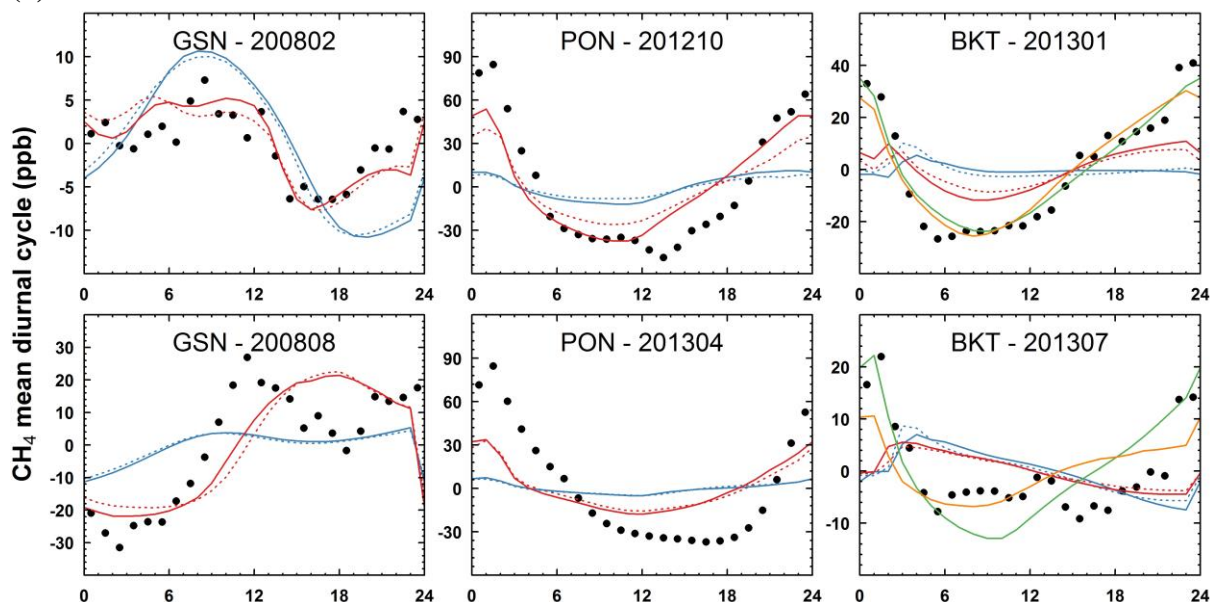
1208

1209

1210

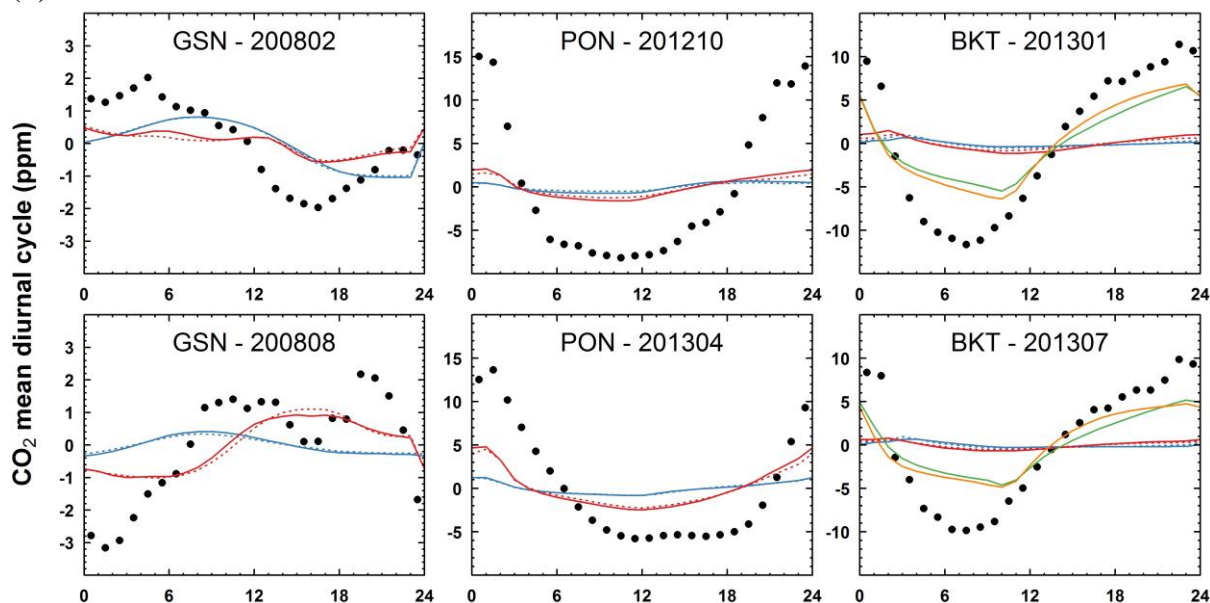
1211 **Figure 5** The observed and simulated mean diurnal cycles (in UTC time) of CH₄ (a) and CO₂
 1212 (b) at three stations within the zoomed region. For BKT, the simulated diurnal cycles at lower
 1213 model levels are also presented.

1214 (a)



1215

1216 (b)



1217

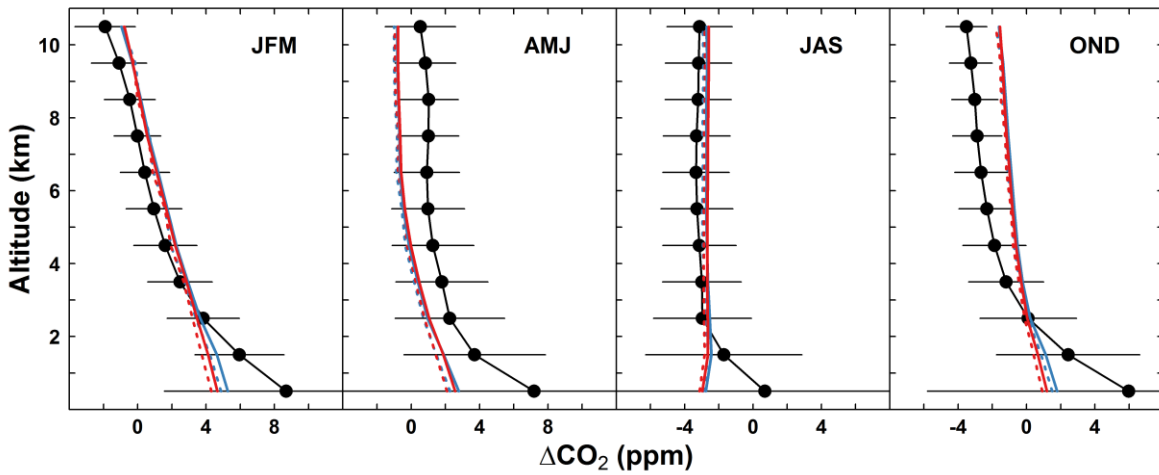
- Observations
- ST19_ED42
- ZA19_ED42
- ST39_ED42
- ZA39_ED42
- ST39_ED42, at lower model level
- ZA39_ED42, at lower model level

1218

1219

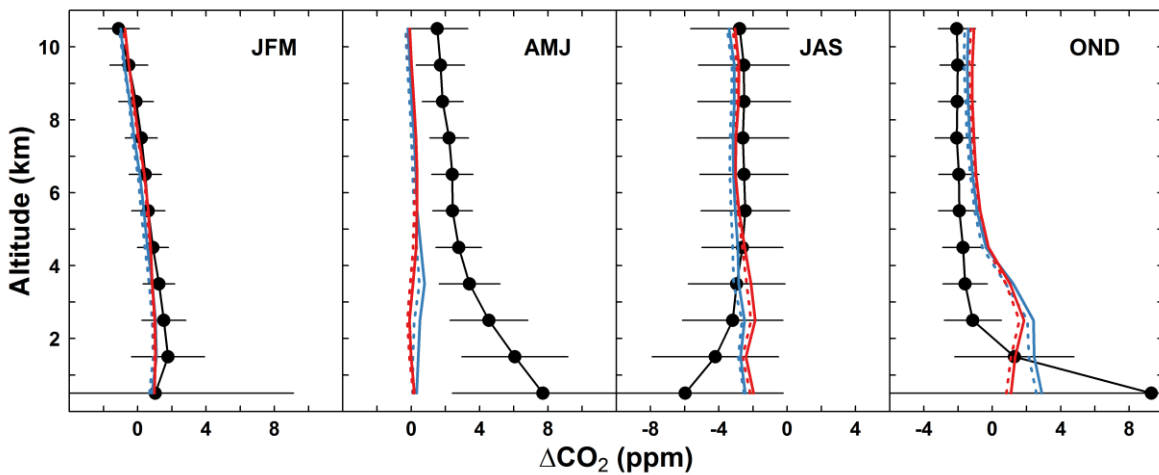
1220 **Figure 6** Seasonal mean observed and simulated CO₂ vertical profiles over (a) East Asia
 1221 (EAS), (b) the Indian sub-continent (IND), (c) Northern Southeast Asia (NSA) and (d)
 1222 Southern Southeast Asia (SSA). The observed vertical profiles are based on CO₂ continuous
 1223 measurements onboard the commercial air flights from the CONTRAIL project during the
 1224 period 2006–2011. For each 1-km altitude bin and each subregion, the observed and
 1225 simulated time series are detrended (denoted as ΔCO_2) and seasonally averaged during
 1226 January–March (JFM), April–June (AMJ), July–September (JAS) and October–December
 1227 (OND).

(a) EAS



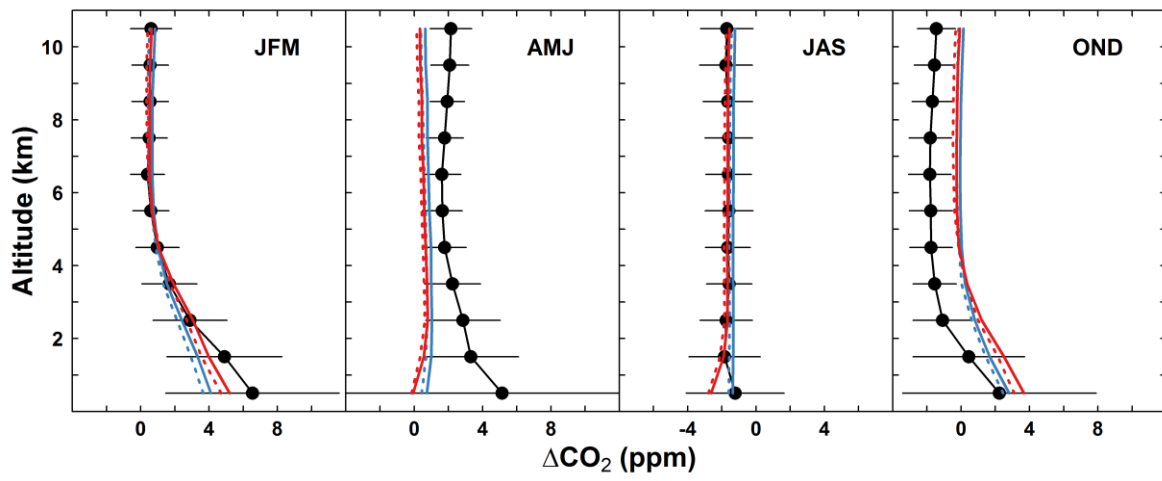
1228

(b) IND



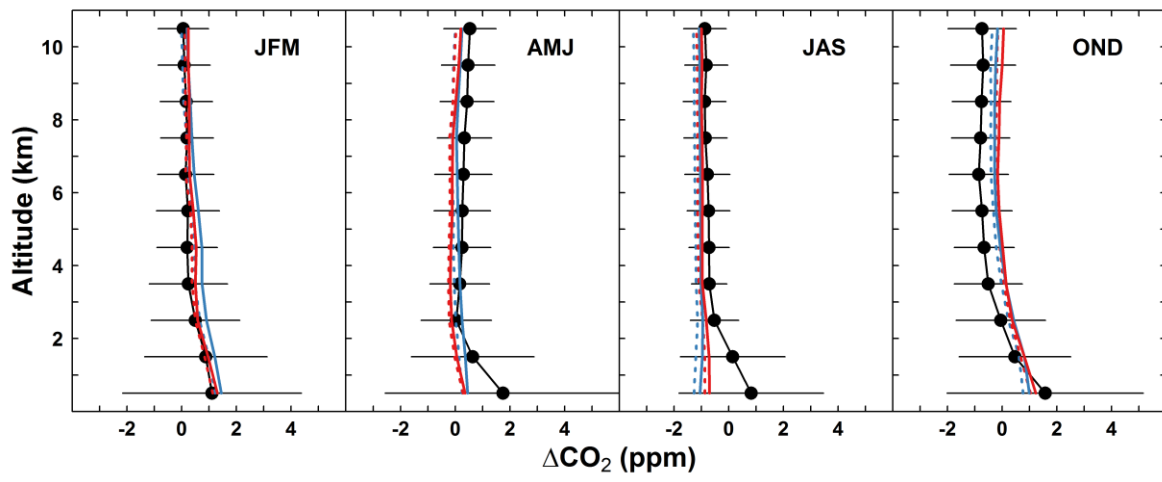
1229

(c) NSA



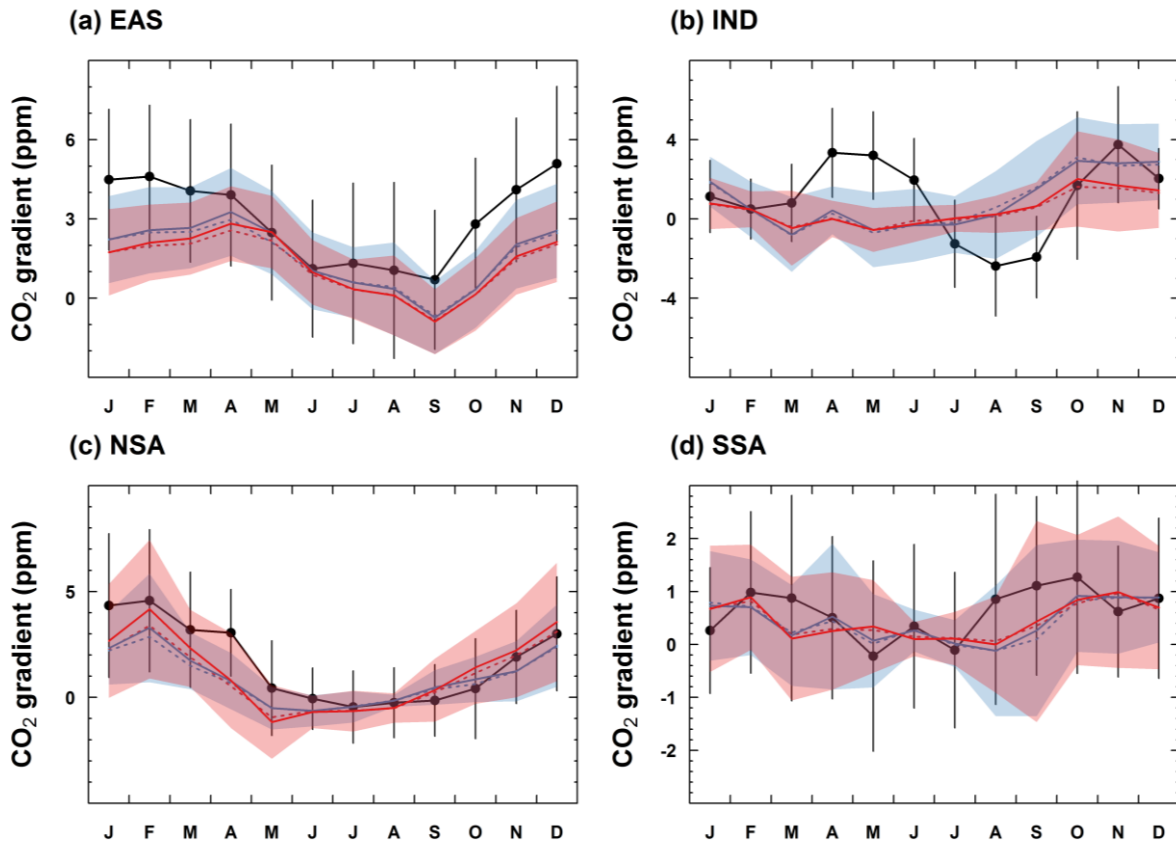
1230

(d) SSA



1231
1232

1233 **Figure 7** Monthly mean observed and simulated CO₂ gradient between 1 and 4km over (a)
 1234 East Asia (EAS), (b) the Indian sub-continent (IND), (c) Northern Southeast Asia (NSA) and
 1235 (d) Southern Southeast Asia (SSA). For each subregion, the monthly CO₂ gradients are
 1236 calculated by averaging over all the vertical profiles the differences in CO₂ concentrations
 1237 between 1 and 4km.



1238

1239

1240